Simultaneous inhibition of natural gas hydrate formation and CO₂/H₂S corrosion for flow assurance inside the oil and gas pipelines

Abdolreza Farhadian,[a*] Yang Zhao,[b] Parisa Naeiji,[c] Alireza Rahimi,[d] Avni Berisha,[e] Lunxiang Zhang,[b*] Zahra Taheri Rizi,[d] Danial Iravani,[f] Jiafei Zhao[b*]

[a] Department of Polymer & Materials Chemistry, Faculty of Chemistry and Petroleum Science, Shahid Beheshti University, GC, 1983969411, Tehran, Iran

[b] Key Laboratory of Ocean Energy Utilization and Energy Conservation of the Ministry of Education, School of Energy and Power Engineering, Dalian University of Technology, Dalian 116023, China

[c] GFZ German Research Centre for Geosciences, Telegrafenberg, 14473, Potsdam, Germany

[d] Faculty of Research and Development of Energy and Environment, Research Institute of Petroleum Industry (RIPI), Tehran, Iran

[e] Department of Chemistry, Faculty of Natural and Mathematics Science, University of Prishtina, 10000 Prishtina, Kosovo

[f] Chemical Engineering Department, Faculty of Engineering, Ferdowsi University of Mashhad, Mashhad, Iran

*Corresponding Authors Email: jfzhao@dlut.edu.cn (J. Zhao), AFarhadian@kpfu.ru, a_farhadian@sbu.ac.ir (A. Farhadian), and lunxiangzhang@dlut.edu.cn (L. Zhang).

Abstract

Compatibility problems are observed during the co-injection of corrosion and gas hydrate inhibitors inside oil and gas pipelines, which reduces their performance. In this study, the newly synthesized dual-purpose inhibitors (DPIs) were developed to overcome the compatibility challenge between the inhibitors. A detailed experimental and computational study was performed to investigate the inhibition activity of DPIs. The results of constant cooling experiments showed that the inhibitors significantly prevented natural gas hydrate formation. DPI2 with a propyl pendant group was the best sample by providing a subcooling temperature of 18.1 ˚C at 5000 ppm. DPI1 and DPI3 decreased gas consumption by 2.6 and 2.4 times, respectively, compared to pure water. In addition, molecular dynamic simulation revealed that the transportation of gas molecules to the growing hydrate cages was disrupted due to DPI2 adsorption on the surface of the hydrate, which partially covered it and acted as a mass transfer barrier. Furthermore, the interaction of the anion part of the inhibitor with the nearest neighbor water molecules lowered the water activity to form the hydrogen-bonding networks for the hydrate formation. According to corrosion measurements, DPIs suppressed the corrosion rate of mild steel in H_2S-CO_2 oilfield-produced water, and the maximum inhibition efficiency of 96.3% was obtained by adding 1000 ppm of DPI2. Moreover, the estimated adsorption energy of DPI2 were relatively high and matched with experimental data, implying that the inhibitor has a high degree of adsorption on the metal for forming a protective layer on the mild steel surface. These findings signified that DPIs provide a potential hybrid inhibition of corrosion and gas hydrate formation for flow assurance applications and reduce the operation costs.

Keywords: Flow assurance, dual-purpose inhibitors, gas hydrates, corrosion, molecular dynamic simulation

1. Introduction

Flow assurance refers to concerns regarding transporting hydrocarbon fluids through pipelines from the reservoir to processing equipment [1]. Flow assurance analysis is critical to deep-water oil and gas exploration and production strategies due to production delays, high remediation costs, and asset damage [2,3]. The major risks to flow assurance are gas hydrate plugging, asphaltene formation, wax deposition, erosion, corrosion, emulsions, and chemical incompatibility problems [3,4]. Controlling gas hydrate plugging is of prime importance among all flow assurance concerns because they form in a shorter timeframe [4,5]. Clathrate gas hydrates are crystalline compounds where light gas molecules, such as methane, ethane, and carbon dioxide, are incorporated inside the molecular cages of water [6]. These compounds are quickly formed inside the pipelines because the thermodynamic conditions inside the pipes are suitable for the formation of hydrates [5]. Thus, the flow of fluid inside the transport flowlines stops due to gas hydrate plugging, leading to economic losses, environmental and safety threats [4,7]. Since the traditional method for gas hydrate inhibition, such as dehydration, lowering pressure, and increasing temperature, are uneconomically methods, chemical treatment using gas hydrate inhibitors has been widely utilized in recent years, especially for gas condensate or gas fields [8–11]. Thermodynamic hydrate inhibitors (THIs) and low-dosage hydrate inhibitors (LDHIs) are the main classes of effective inhibitors [12–14]. THIs, such as glycol compounds, methanol, and some inorganic salts at high concentrations (<20%), mainly affect the chemical activity of water and change the equilibrium phase of hydrate formation [15,16]. The exacerbation of corrosion, impact on hydrocarbon quality, storage tank requirement and regeneration equipment, flammability, and toxicity of methanol are the technical challenges of using THIs [4,17]. LDHIs are divided into two categories, namely kinetic hydrate inhibitors (KHIs) and anti-agglomerants (AAs) hydrate inhibitors [18–20]. KHIs

are water-soluble polymers containing imide or amide functional groups, and they are typically used at 0.1-2 wt.% [21–23]. Poly(N-vinyl lactam)s, poly(N-isopropylacrylamide), polyvinylpolypyrrolidone, poly(N-alkyl (meth)acrylamide)s, and hyperbranched polyesteramide are commercially available KHIs [24–26]. The mechanism action of KHIs is predominantly on the kinetics of gas hydrate formation by delaying nucleation and crystal growth of hydrates [27–29]. Unlike KHIs, AAs, including quaternary salts of phosphonium and ammonium, mainly do not affect hydrate formation kinetics [30,31]. Gas hydrates are formed in the presence of AAs, but they inhibit the agglomeration of hydrate crystals [31–33]. Thus, hydrate particles are transported as a nonstick slurry inside the pipelines [34,35].

Corrosion is another major economic and flow assurance concern as it is the most widespread destructive phenomenon in the oil and gas industry [36–38]. Low-carbon steel is commonly used as the structural material for transportation pipelines due to its good mechanical properties and cost-effectiveness [39–42]. However, the presence of acid gases, such as H_2S and CO_2, in natural gas causes the corrosion of steel-based pipelines [43–45]. Although H_2S corrosion is more severe than CO_2 corrosion, the predominant type of corrosion in the industry is in the CO_2-containing medium [46–48]. On the other hand, a mixture of H_2S and CO_2 strongly attack the steel in the production and transportation of gas and oil [49]. Besides, the trapping of H_2S and CO_2 in hydrate deposits increases the corrosion rate of steel more than free gases. Moreover, a higher concentration of the gases forms during gas hydrate dissociation, which intensifies the corrosion process [50].

Like gas hydrate management, applying organic compounds as corrosion inhibitors is the most effective method of preventing steel corrosion [41,51]. According to the literature, imidazoline-based compounds are the most effective corrosion inhibitors for H_2S and CO_2 corrosion [51].

Although the usage of inhibitors prevents corrosion and gas hydrate formation inside the pipeline, incompatibility problems between inhibitors are observed during their simultaneous injection into flowlines [52]. According to the literature some surfactant-based corrosion inhibitors significantly reduce the performance of KHIs and vice versa [17,53,54]. Incompatibility problems can be caused by the KHI-corrosion inhibitor interactions and the preferred absorption of hydrate inhibitors on the pipe wall [55,56]. Moreover, many surfactants, especially their anionic type with good emulsifying or foaming properties enhance the formation of gas hydrate [57]. Thus, develop of a single inhibitor that work as dual-purpose inhibitors (DPIs) for simultaneous suppression of corrosion and gas hydrate formation is a good solution to this problem, resulting in considerable economic savings [58]. In recent years, ionic liquids, amino acids, biomolecules, and copolymers of vinyl caprolactam have been investigated as DPIs; however, their inhibition activity on gas hydrate is not desirable and some of them are expensive [58]. Herein, novel waterborne polyurethanes containing the active groups for mitigation of both gas hydrate and corrosion were synthesized as efficient DPIs. The inhibition effect of DPIs on natural gas hydrate formation and mild steel corrosion were assessed using a high-pressure vessel and electrochemical techniques in H_2S-CO_2 medium, respectively. Moreover, the mechanism action of DPIs on gas hydrate formation was clarified using a simulation study.

2. Experimental section

2.1. Materials

Synthetic natural gas (SNG) with composition of methane (80.67%), ethane (10.20%), propane (4.90%), iso-butane (1.53%), n-butane (0.76%), nitrogen (0.10%), and carbon dioxide (1.84%) was supplied by Dalian Special Gases Co., Ltd. 3-Mercaptopropane-1,2-diol, N-vinylcaprolactam (VCap), N,N-dimethylformamide (DMF), triethylamine, toluene diisocyanate (TDI), 2,2-

bis(hydroxymethyl)propionic acid, 1,2-Pentanediol, 1,2-Butanediol, polyethylene glycol (PEG 400), and 2-Ethyl-1,3-hexanediol were purchased from Sigma Aldrich. Electrochemical measurements were performed using mild steel (MS) coupons with composition of (wt.%) C, 0.145; Ti, 0.003; Mn, 0.988; Ni, 0.016; B, 0.001; Co, 0.005; Pb, 0.003; Si, 0.022; W, 0.007; V, 0.045; Sn, 0.004; Ta, 0.008; Al, 0.044; Mo, 0.015; P, 0.015; As, 0.012; Cr, 0.043; Nb, 0.001; Zn, 0.002, S, 0.003; Cu, 0.052 and Fe for balance.

2.2. Synthesis of DPIs

A diol was synthesized based on VCap using the thiol-ene "click" reaction in quartz tubes [59,60]. Briefly, 20 g (0.143 mol) VCap and 12.43 mL (0.143 mol) 3-Mercaptopropane-1,2-diol dissolved in 30 mL of DMF and transferred to the quartz tubes. The reaction was performed under UV irradiation (365 nm) at room temperature for 16 h. Then, the solvent was evaporated, and the obtained diol (Scheme. S1) was used for the preparation of DPIs. Three DPIs with different alkyl chains were prepared according to our group's previous work [13,30,52]. Molecular structure of DPIs is shown in Fig. 1. ^{1}H NMR of DPI1; ^{1}H NMR (300 MHz, DMSO) δ 9.58 (s, 0H), 9.01 – 8.80 (m, 0H), 7.94 (s, 2H), 7.19 (s, 1H), 7.08 (d, *J* = 17.9 Hz, 1H), 6.08 (s, 5H), 4.88 (q, *J* = 7.6 Hz, 0H), 4.23 (s, 2H), 4.08 – 3.95 (m, 1H), 3.48 – 3.31 (m, 1H), 3.07 – 2.96 (m, 1H), 2.87 (d, *J* = 2.9 Hz, 5H), 2.72 (d, *J* = 2.9 Hz, 5H), 2.67 – 2.54 (m, 1H), 2.18 (s, 2H), 2.12 (s, 1H), 1.66 – 1.58 (m, 0H), 1.54 (s, 1H), 1.39 (s, 1H), 1.33 – 1.07 (m, 5H), DPI2; ^{1}H NMR (300 MHz, DMSO) δ 9.58 (s, 0H), 9.02 – 8.72 (m, 0H), 7.94 (d, *J* = 3.0 Hz, 4H), 7.20 (s, 1H), 7.05 (s, 1H), 5.49 (s, 6H), 4.23 (s, 1H), 4.08 – 3.94 (m, 1H), 3.50 – 3.31 (m, 1H), 3.09 – 2.93 (m, 1H), 2.76 – 2.68 (m, 12H), 2.57 – 2.47 (m, 1H), 2.19 (s, 1H), 2.12 (s, 1H), 1.58 – 1.51 (m, 1H), 1.45 – 1.25 (m, 1H), 1.30 – 1.18 (m, 2H), 1.23 – 1.08 (m, 2H), 0.86 (dq, *J* = 7.2, 3.2 Hz, 1H), and DPI3; ^{1}H NMR (300 MHz, DMSO) δ 9.58 (s, 0H), 8.87 (d, *J* = 6.6 Hz, 0H), 8.47 – 8.26 (m, 1H), 7.94 (s, 5H), 7.25 – 7.15 (m, 1H), 7.14 – 7.00 (m, 1H), 5.97 (s, 5H), 4.24 (s, 1H), 4.07 – 3.94 (m, 1H), 3.88 – 3.54

(m, 1H), 3.58 – 3.38 (m, 1H), 3.34 – 3.09 (m, 2H), 3.14 – 2.92 (m, 4H), 2.72 (d, J = 2.5 Hz, 15H), 2.61 (d, J = 8.7 Hz, 1H), 2.58 – 2.32 (m, 2H), 2.27 – 2.07 (m, 3H), 1.68 – 1.46 (m, 1H), 1.46 – 1.05 (m, 6H).
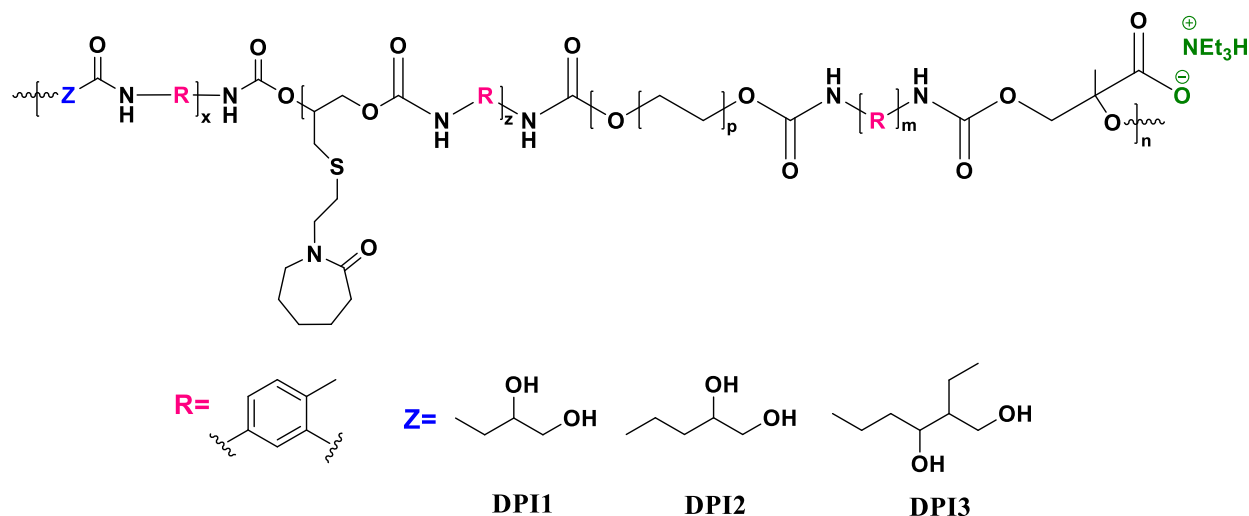
Fig. 1. Chemical structure of DPIs.

2.3. Gas hydrate formation experiments

A high-pressure vessel was used to assess the inhibition effect of DPIs on gas hydrate formation (Scheme. S2). For each experiment, 100 mL of pure water or DPI solution was poured into the cell. Then, SNG was injected to the cell to eliminate air, the cell was pressurized to 6.5 MPa at 25 ˚C, and stirring was set to 400 rpm. After the equilibrium of liquid and gas phases, the temperature of the system was decreased from 25 ˚C to 1 ˚C at a 3 ˚C/h rate. Subsequently, the temperature was kept at 1 ˚C to detect an obvious indicator of hydrate formation. The onset temperature and induction time of hydrate formation were monitored using pressure transducer (GE Druck, accuracy ± 0.02%) and temperature sensor (PT-100). The induction time was expressed as the time from the beginning of the test until a sudden drop in pressure observed or temperature fluctuated during the process.

2.4. Corrosion study

The potential of DPIs to prevent MS corrosion in H_2S-CO_2 oilfield-produced water was evaluated using IM6-ex, ZAHNER Electrik instrument. Oilfield-produced water was used for all corrosion experiments [52]. After removing oxygen inside the solution, H_2S and CO_2 were injected to attain a saturated solution. Once open circuit potential (OCP) was stabled, potentiodynamic polarization (PDP) experiments were conducted from -200 mV to +200 mV at a potential sweep rate of 0.5 mV s^{-1} relative to OCP. Electrochemical impedance spectroscopy (EIS) tests were performed in the frequency range from 100 kHz to 0.01 Hz with a peak-to-peak amplitude of 10 mV. All measurements were performed three times under dynamic conditions.

3. Results and discussion

### 3.1. High-pressure vessel results

This study used SNG as a structure II-forming gas because it is the most thermodynamically stable phase in the oil and gas fields [61]. The determination of the induction time is not repeatable, and uncertainty often is observed in the results because the nucleation of gas hydrate crystals is a stochastic process [4]. Thus, the constant cooling method was used to measure the onset temperature of gas hydrate formation. Before the experiments, the equilibrium temperature (T_{eq}) for SNG hydrate was theoretically calculated using CSMGem software at different temperatures [7]. The pressure-temperature curve for SNG hydrate is displayed in Fig. 2a. This curve provides valuable information for gas hydrate formation to predict subcooling temperature, hydrate-free, and stable hydrate regions. The difference between hydrate stability and operating temperatures at a given pressure is expressed as subcooling temperature (ΔT) [7]. As seen in Fig. 2a, the value of T_{eq} for the sII-forming gas at 6.5 MPa is 19.03 ˚C. It means that the SNG hydrate is formed below this temperature. Hence, DPIs have good inhibition power if they prevent hydrate formation at lower temperatures than T_{eq} (Higher ΔT).
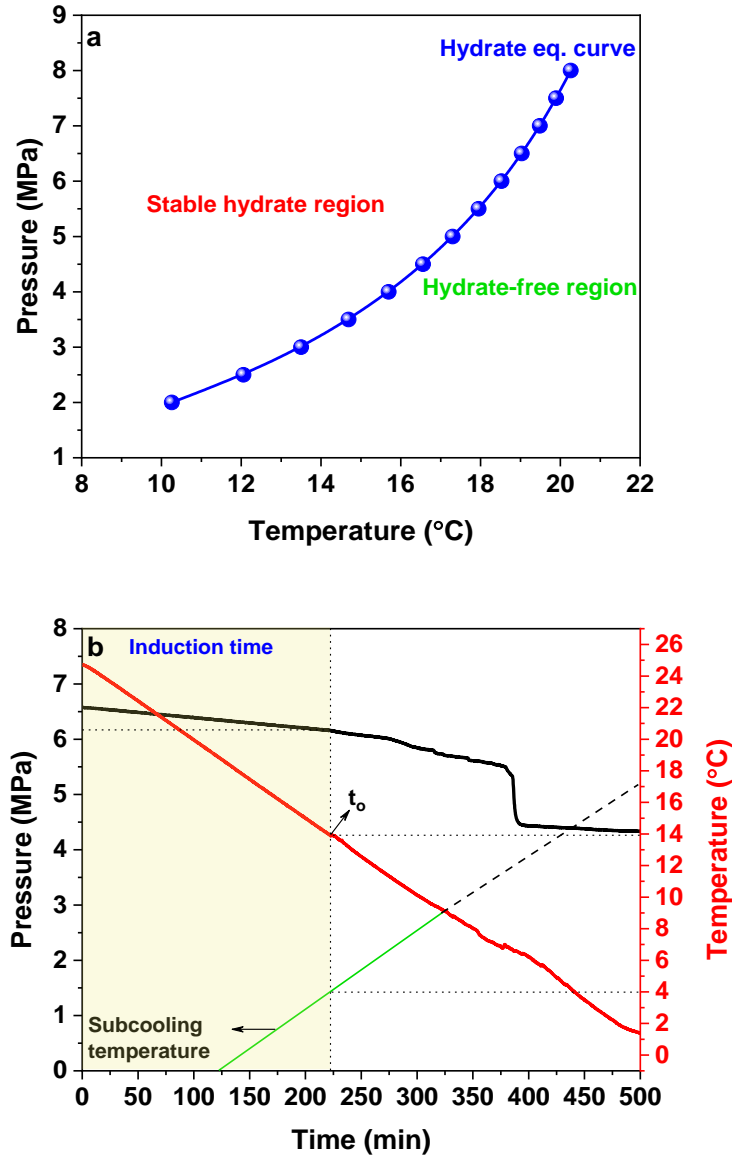
Fig. 2. Pressure–temperature curve for SNG hydrate (a) and an example of T_o and subcooling temperature determination in pure water solution (b).

In addition, Fig. 2b shows a typical pressure-temperature curve obtained from the constant cooling experiment for the pure water system used to determine the onset temperature (T_o). The pressure inside the cell linearly decreases by lowering the temperature from 25 ˚C to 1 ˚C because the system is close during the test. The value of T_o is determined by the first sudden drop in pressure,

indicating the temperature at which the first macroscopic formation of gas hydrates is detected [23,28,62]. The results from a high-pressure vessel for different concentrations of DPIs are represented in Fig. 3 and Table 1. In this study, the value of T_o was mainly discussed because it is the most useful parameter for field applications [62]. According to the literature, a KHI with a larger alkyl chain can show better inhibition efficiency if its solubility in water is preserved [63,64]. In addition, it has been reported that the inhibition performance of KHIs with n-propyl groups was more than the iso-propyl group [65,66]. As seen in Table 1, DPI1 with ethyl side groups significantly suppressed the nucleation of SNG hydrate compared to pure water. A solution containing 2500 ppm of DPI1 decreased the value of T_o from 13.94 ˚C in the uninhibited system to 9.69 ˚C, which is equal to ΔT= 9.4 ˚C. The inhibition power of DPI1 was further improved by increasing its concentration to 5000 ppm, as is seen in Fig. 3. The inhibitor effectively inhibited the formation of SNG hydrate up to 6.01 ˚C, providing a ΔT value of 13.0 ˚C. Table 1 reveal that DPI2 with a larger alkyl chain (propyl group) showed an excellent inhibitory performance. DPI2 lowered the onset temperature of SNG hydrate formation to 0.9 ˚C at 5000 ppm with an average ΔT value of 18.1 ˚C. Generally, most of the commercial KHIs provide a maximum subcooling of 9-10 ˚C for sII-forming gas [4]. Therefore, such a high ΔT (18.1 ˚C) is very impressive for a KHI and indicate that it is very powerful to prevent the formation of gas hydrates. However, with further increase of hydrophobic groups in the structure of DPI3, its inhibitory activity decreased, and only a ΔT value of 6 ˚C was observed. It might be due to steric hindrance between the branched substituent and polymer chains in DPI3, suggesting propyl groups are the suitable size of the alkyl group for a good performance of DPIs.
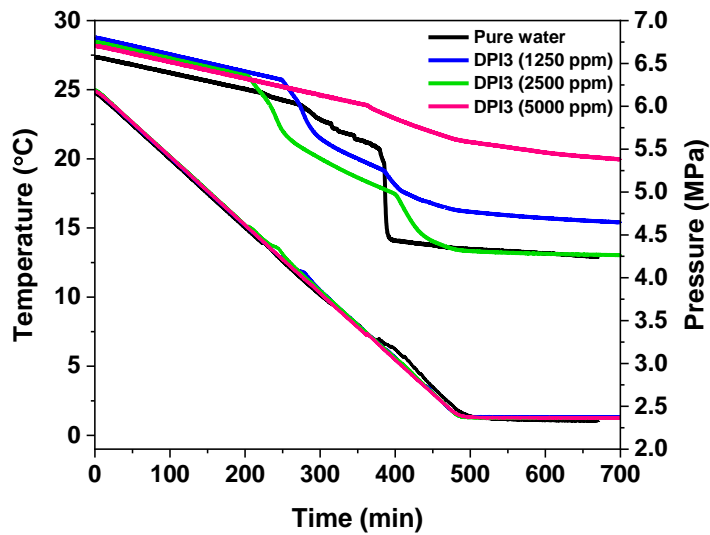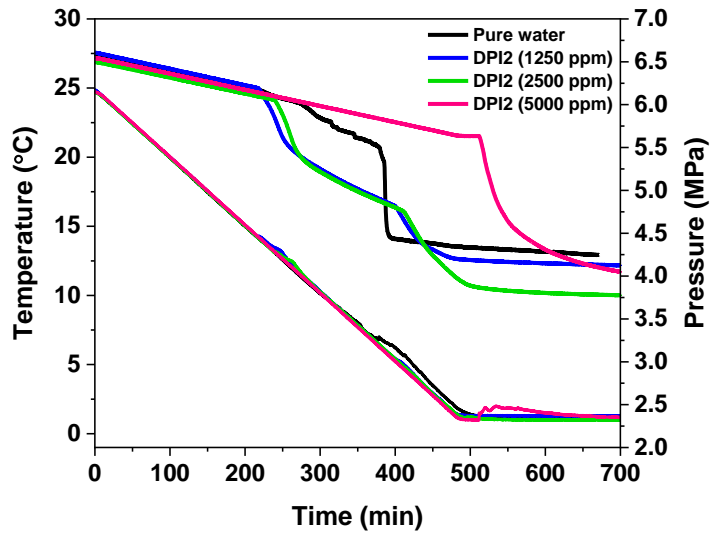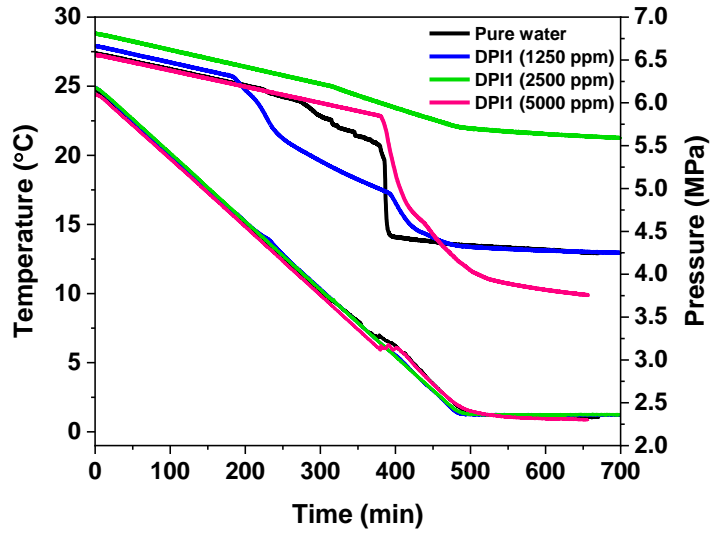
Fig. 3. Pressure-temperature curves obtained from the constant cooling method for pure water and DPI solutions.

Table 1. Hydrate formation temperatures and pressures in the absence and the presence of DPIs.

Sample	Concentration (ppm)	Hydrate onset pressure (MPa)	T_o (°C)	ΔT (°C)	Gas consumption (%)
Pure water	-	6.16	13.94	5.1	25.17
DPI1	1250	6.30	14.03	5.0	27.94
	2500	6.20	9.69	9.4	9.60
	5000	5.85	6.01	13.0	33.56
DPI2	1250	6.20	14.13	5.0	28.70
	2500	6.07	12.98	6.1	33.09
	5000	5.63	0.90	18.1	34.56
DPI3	1250	6.31	13.05	6.0	23.82
	2500	6.35	15.15	3.9	28.32
	5000	6.02	13.19	5.9	10.31

Moreover, the amount of gas consumption in pure water and DPI solutions was calculated using Eq. (1) to study the effect of the inhibitors on the growth step of SNG hydrate crystals [54,55].

$$\alpha = \frac{P_h - P_r}{P_h} \times 100 \tag{1}$$

Where P_r and P_h are the actual pressure in the cell at a given time and the hypothetical pressure at the beginning of the test, respectively. The results of gas consumption in different systems are presented in Table 1 and Fig. 4. Furthermore, the appearance of SNG hydrate formed in pure water and DPIs are depicted in Fig. 5. Table 1 exhibits that DPIs have a different effect on SNG hydrate formation. For example, DPI2 showed the best inhibition activity on the nucleation step of hydrate crystals as it delayed their formation by a ΔT value of 18.1 °C at 5000 ppm.
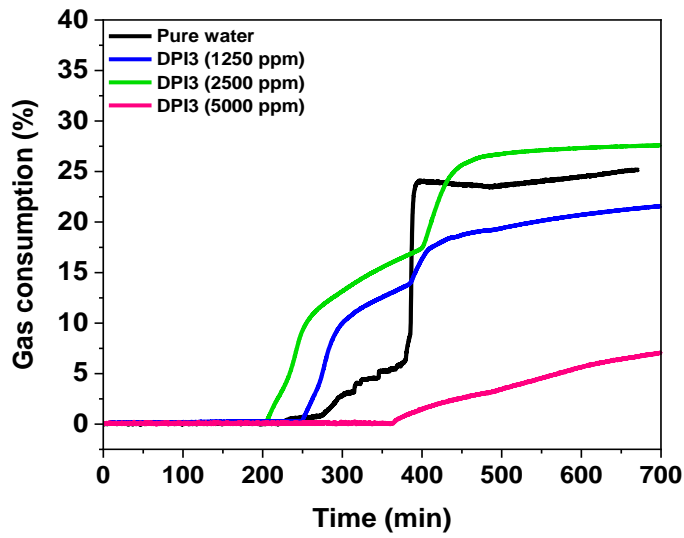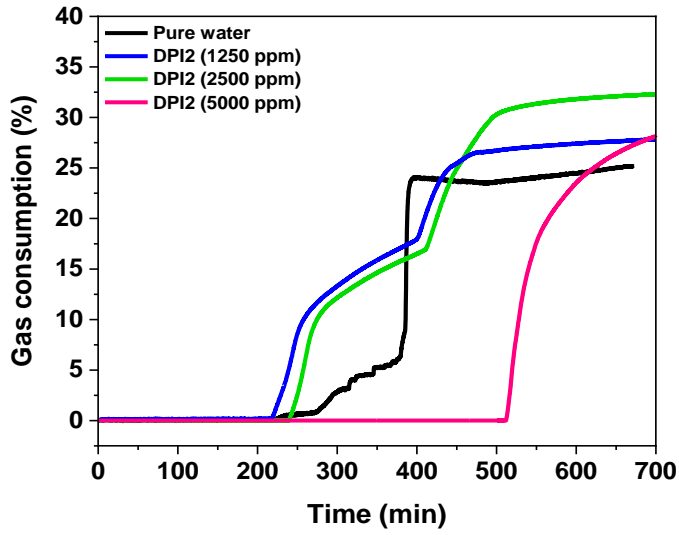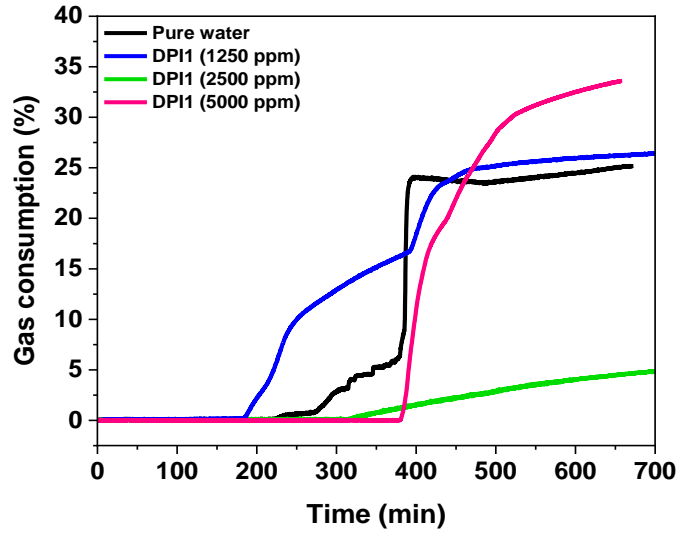
**Fig. 4.** Gas consumption ratio curves for pure water and DPI solutions.

In contrast, DPI3 had a lower inhibition effect on the nucleation of hydrate than DPI2, but it considerably inhibited the growth of SNG hydrate. DPI3 decreased gas consumption from 25.17% in a pure water system to 10.31% at 5000 ppm. DPI1 acted as a good inhibitor for the nucleation and growth of SNG hydrate crystals. It provided a ΔT value of 13.0 ˚C and reduced gas consumption by 2.62 times compared to pure water (Fig. 5). Hence, it can be concluded that the prominent inhibition effect of DPI3, DPI2, and DPI1 is on crystal growth, nucleation of hydrate, and the whole process of SNG hydrate formation, respectively. A possible reason for the good inhibitory activity of DPIs is that they contain efficient components for gas hydrate inhibition, including the caprolactam ring, alkyl chains, many heteroatoms, and urethane bonds. DPIs can interact with water molecules through amide, urethane bonds, and heteroatoms to form new hydrogen bonds and reduce available water to form hydrate. Besides, the alkyl chains of DPIs disrupt the water cavities and inhibit the crystal growth of SNG hydrates [65,67].
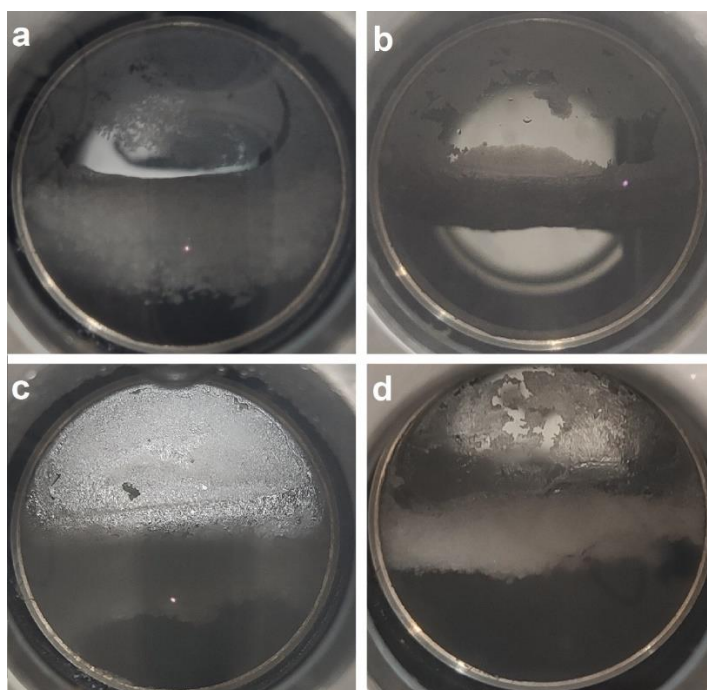
Fig. 5. SNG hydrate formed in pure water (a), DPI1 (b), DPI2 (c), and DPI3 (d) solutions after constant cooling experiments.

*3.3. Mechanism of gas hydrate inhibition*

The molecular dynamic simulation was performed to show the exact role of DPI molecules in the hydrate growth and its behavior at the hydrate surface. The initial configuration of the simulation boxes is shown in Fig. 6a. One molecule of DPI2, as the best sample, was placed to the right of the liquid phase to examine the inhibitor's effect on the surface of hydrate and compare it to what occurs on the uninhibited side of the surface. Fig. 6b indicates the molecular structure of DPI2.
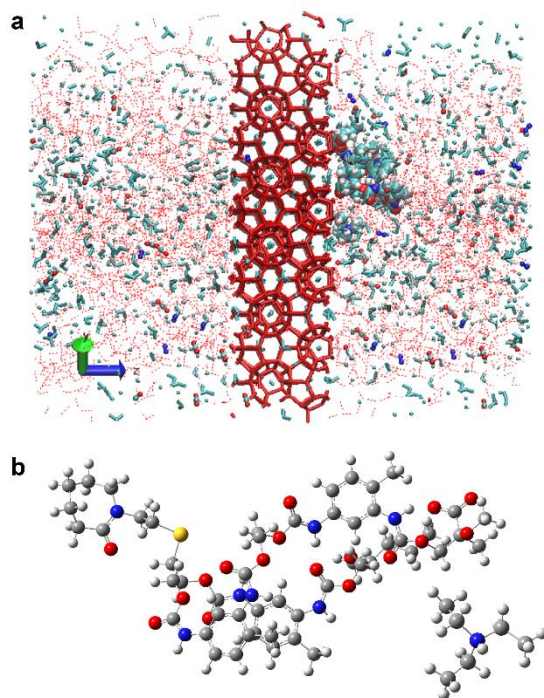
Fig. 6. Initial configuration of the simulation box (a). The molecular structure of the additive (b). Methane molecules, nitrogen, sulfur, carbon, hydrogen, and oxygen atoms are shown with green, blue, yellow, cyan, white and red colors, respectively.

Fig. 7 shows the snapshots of the sII hydrate growth simulation on the (110) surface. During the simulation, the migration of gas molecules to the interfaces of hydrate and solution caused the hydrate growth due to the order of water molecules around those gas molecules in the neighborhood of the hydrate interface. The hydrogen bond network involving water around the gas molecules makes a stable hydrate structure. As seen in the figure, the right-side interface of the hydrate phase was exposed to one DPI2 molecule, and therefore it would be expected to have a different growth process at two hydrate interfaces. For more clarification, the hydrogen bonding of the hydrate slab and the solutions were differentiated in terms of color. Hydrate crystals grew gradually up to 20 ns on both sides. However, more hydrate cages formed in the left-side interface due to a higher tendency to order the water molecules around the gas molecules. While the presence of DPI2 close to the right-side interface prevented the formation of the hydrogen-bonding networks. It can be seen that one layer of the hydrate could not even be completed on the right-side solution phase.
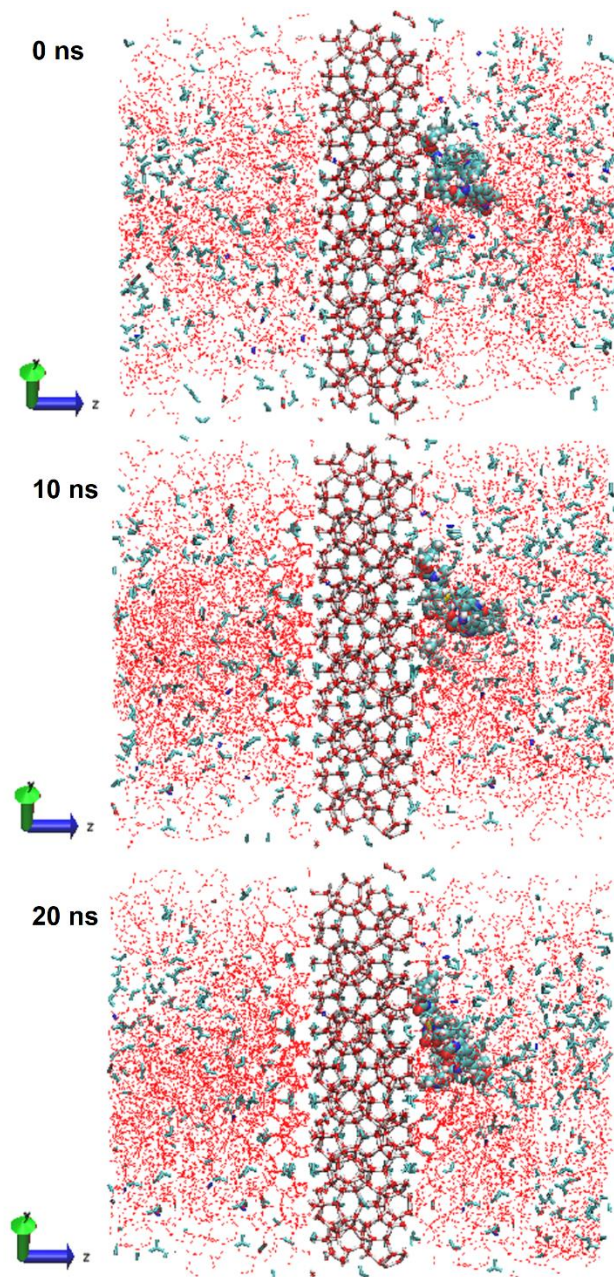
Fig. 7. Snapshots of sII mixed gas hydrate growth on the (110) surface over simulation time. Red and pink colors, respectively, show the hydrate bonding in the hydrate and solution phases.

Furthermore, Fig. 8 displays DPI2 configurations on the (110) and (001) surfaces over simulation time. The large anionic part of the DPI2 molecule stays close to the hydrate surface, while the cationic part of the molecule tends to remain in the bulk solution. The orientation of the anionic

part of the inhibitor during the simulation showed that it tends to be stretched along the hydrate surface and adsorbed on it. The transportation of gas molecules to the growing hydrate cages was disrupted due to DPI2 adsorption on the surface of the hydrate, which partially covered it and acted as a mass transfer barrier [68]. The time-lapse snapshots showed that DPI2 has a lower tendency to form the hydrate cages and that the incomplete hydrate cages might be disturbed by the inhibitor. Therefore, the results visually demonstrated that DPI2 has a significant inhibition effect on gas hydrate formation. The following calculations could help to quantify this statement well. The F_3 order parameter was calculated for different cross-sections of the slab of the simulation cell perpendicular to the z-direction. Fig. 9a demonstrates the variation of this parameter over time for the layers of L_1, L_2, H, R_1, and R_2 of the simulation box, so that they indicate the left-side (L_1 and L_2) and right-side (R_1 and R_2) solutions of the hydrate phase (H). It is clear that the value of F_3 parameter for layers L_2 and R_2, which are away from the growing crystal surface, remains almost constant at around 0.065 with some fluctuations. It confirms that the water molecules at these layers are in a liquid-like amorphous phase. In addition, layer H showed a nearly constant value of about 0.007 for F_3 parameter implying the water molecules were arranged into the hydrate structure. However, despite the F_3 value for layers L_2, R_2, and H remaining nearly unchanged during the simulation, F_3 parameter of layers L_1 and R_1 gradually decrease since they are the closest layers to the hydrate slab. At the early stage of the hydrate growth, the partial cages on the interfaces start to get completed, and thus the F_3 value was dropped quickly. Then, the liquid water began to rearrange into an orderly hydrate crystal structure, and decreasing the F_3 value continued until the end of the simulation. The goal is to compare the decreasing rate of the F_3 value for layers L_1 and R_1 because DPI2 was located in one of them.
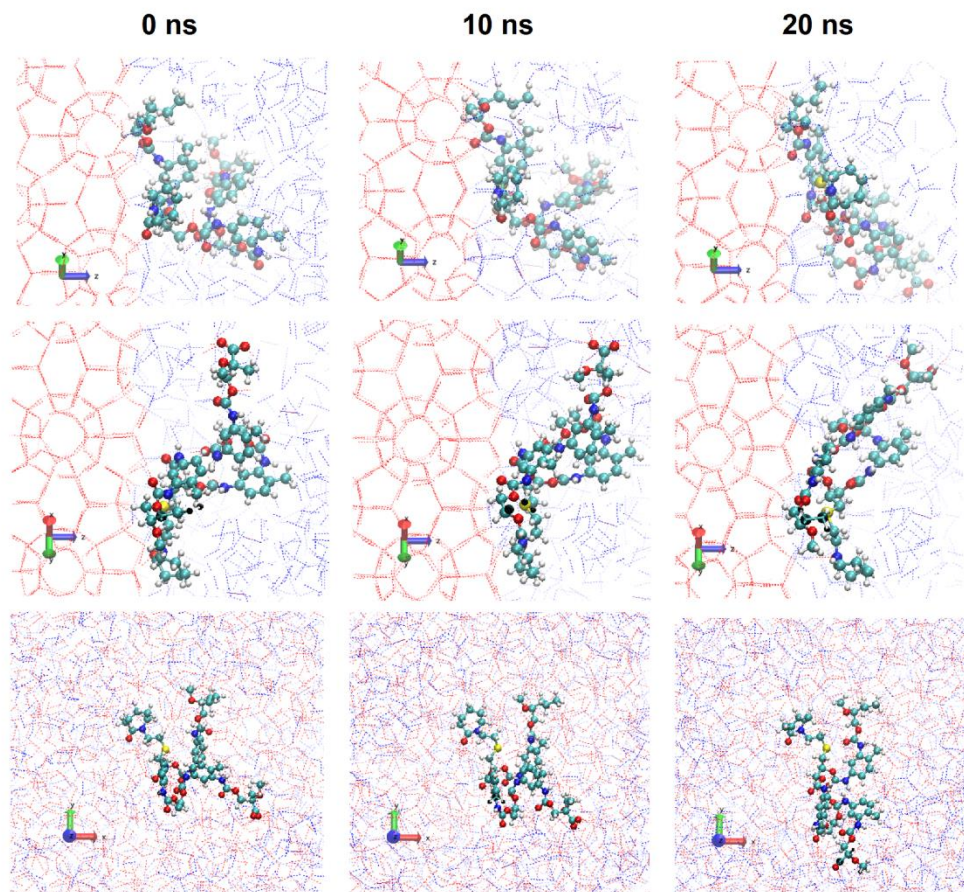
Fig. 8. The configurations of DPI2 molecule during the simulation on the surfaces (110) and (001). The water molecules in the initial hydrate phase are presented in red hydrogen bonding lines.

As seen in Fig. 9a, the F_3 order parameter of layer L_1 decreased faster than that of layer R_1. After around 20 ns, a value of ~0.03 was obtained for the F_3 of layer L_1, while this value was approximately 0.05 for layer R_1. It can be concluded that the DPI2 prevented hydrate growth process by disrupting the order of water molecules to form hydrate networks.
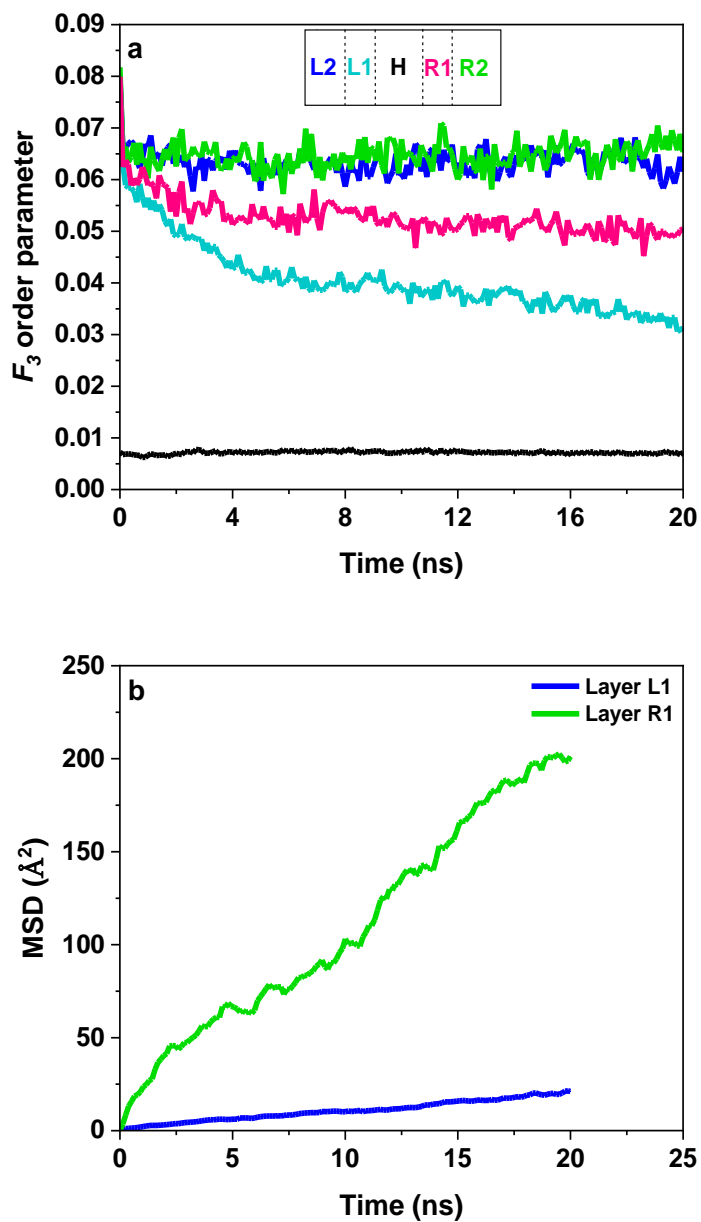
Fig. 9. F_3 order parameter of sII mixed gas hydrate growth in the different slabs of the simulation box in the presence of a DPI2 molecule (a). The layers of L_1 and R_1 have a thickness of ~18 Å. Variation of MSD at the layers of L_1 and R_1 during the simulation (b).

MSD was calculated for the molecules at L_1 and R_1, which are the closest layers to the hydrate surfaces, and is shown in Fig. 9b. The mobility of the free water and gas molecules in the local

environment may be affected by the conversion of the water molecules from the liquid-like to the solid-like for forming the hydrate cages and the gas molecules involved in these cages. Thus, a reduction in the value of MSD is observed. The diffusion coefficient of the diffusing atoms is proportional to the slope of the MSD versus time. Comparing MSD for two layers illustrates that layer L_1 showed a lower MSD slope than another one. It indicates that the hydrate growth has a faster rate in the layer free of DPI2, while R_1 can be affected by the inhibitor due to the slower hydrate growth rate. Therefore, the molecules can diffuse and move more accessible and faster. As known, the injection of an inhibitor indirectly eliminates the free water when much of the free water is hydrogen-bonded to it. In this condition, the water activity is decreased, and more severe thermodynamic conditions are required for hydrate formation at lower concentrations of free water [7]; however, it is not sometimes the structural property solely responsible for inhibition activity [68]. Therefore, it is good to know whether the additive can be involved in hydrogen bonding with water molecules and how strong it is. If the distance between the donor atom (D) and acceptor atom (A) is less than the cutoff distance (3.0 Å), and the angle of D-H-A is less than the cutoff angle (20˚), a hydrogen bond is formed between them. Fig. 10a exhibits the number of hydrogen bonds of water molecules with DPI2 during the simulation. This signifies that hydrogen bonds are formed between DPI2 and the nearest neighboring water molecules. A stronger proton-accepting hydrogen bond suggests that DPI2 tends to accept the proton from the free water, disrupting the incomplete hydrogen bonding networks formed by the water molecules, and/or lowering the water activity to form such networks. Moreover, the strength of the acceptor atoms of DPI2 was compared together. The oxygen atoms in the single (ether group) and double bonds (carbonyl group) and nitrogen atoms of the inhibitor were considered the acceptor of water's protons. Fig. 10b illustrates that the oxygen carbonyl group can form the strongest hydrogen bonds with water

molecules. There is visual evidence of hydrogen bonding between DPI2 and free water molecules when it is a proton acceptor. Fig. 11 shows some interactions between water molecules and the inhibitor atoms close to the hydrate surface. It confirms the interaction of DPI2 with the water molecules around it by forming hydrogen bonds, as shown by the black blocks.
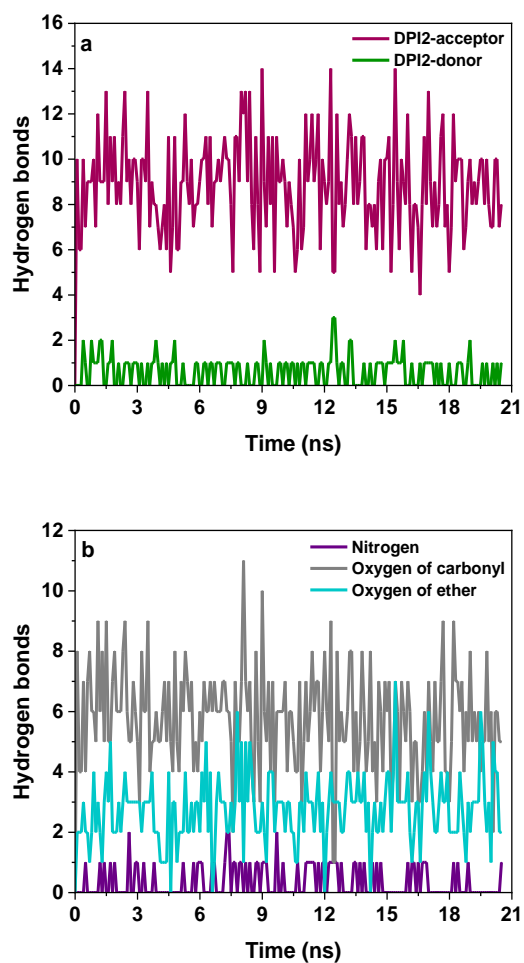
Fig. 10. The number of hydrogen bonds between DPI2 and water molecules (a) and the acceptor atoms of DPI2 and protons of water molecules (b).
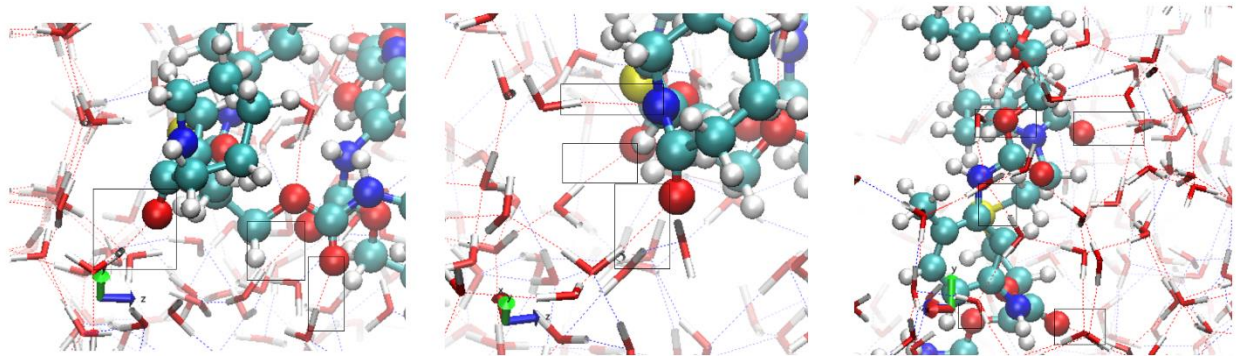
Fig. 11. The formation of hydrogen bonds between DPI2 and water molecules of the hydrate cages (black blocks).

3.4. Corrosion studies

3.4.1 Potentiodynamic polarization study

Before all electrochemical measurements, the variation of open circuit potential (OCP) of MS was recorded over 60 min. The OCP curves for blank and DPI media are shown in Fig. S1. The figure indicates that the potential of the systems reached equilibrium after 40 min, and the value of OCP in the presence of DPIs was more positive than blank, especially at the beginning of the measurement. Such a positive shift in the OCP curves suggests that the susceptibility of MS to dissolution in H_2S-CO_2 solution was decreased due to the adsorption of DPIs on the metal surface [69,70]. To investigate the inhibition activity of MS corrosion in H_2S-CO_2 oilfield-produced water, PDP experiments were carried out as a direct current method. PDP curves of MS in the aggressive medium for blank and DPI solutions are depicted in Fig. 12. As seen in the figure, anodic and cathodic reactions on the surface of MS are affected in the presence of DPIs, and the corrosion potential (E_{corr}) is displaced toward both positive and negative directions. The maximum observed shifts in E_{corr} for DPI1, DPI2, and DPI3 are 34 mV, 31 mV, and 32 mV, respectively. Therefore, DPIs can be classified as mixed-type corrosion inhibitors as the changes in E_{corr} is lower than 85

mV [46]. The PDP parameters, such as corrosion current density (i_{corr}), Tafel slopes (βa, βc), corrosion rate (CR), polarization resistance (R_p), and $E_{corr,}$ are calculated by Tafel extrapolation (Table 2). In addition, the inhibition efficiency value (η_{PDP}%) of DPIs were calculated using Eq. (2) [40,52,71]:

$$\eta_{PDP} = \frac{i^0_{corr} - i_{corr}}{i^0_{corr}} \times 100 \qquad (2)$$

where i^0_{corr} and i_{corr} represent, respectively, the corrosion current densities for blank and DPIs systems. According to Table 2, adding DPIs to the corrosive solution significantly suppressed the corrosion of MS. DPIs improved the resistance to a polarization of MS up to 7.32 kΩ cm^2 compared to a blank (0.44 kΩ cm^2). The corrosion rate decreased from 18.90 mpy in the uninhibited system to 1.11 mpy, 0.70 mpy, and 1.34 mpy in solutions containing 1000 ppm of DPI1, DPI2, and DPI3, respectively. The inhibitors prevented H$_2$S-CO$_2$ corrosion by adsorbing the active sites of the MS surface. DPIs can exchange free electrons via their heteroatoms and π–bonds within the aromatic groups with Fe atoms. Therefore, they reduce the transfer of electrons from the cathodic to the anodic site. Moreover, DPIs electrostatically interact with Cl$^-$ ions that are initially adsorbed on the surface of MS due to the generation of Fe^{2+}. Thus, the value of i_{corr} considerably lowered from 41.38 μA cm^{-2} in blank solution to 1.53 μA cm^{-2} in the presence of DPI2. These results indicate that DPIs can be considered efficient inhibitors for mitigating MS corrosion in H$_2$S-CO$_2$ oilfield-produced water as the maximum η values of 94.2%, 96.3%, and 92.9% achieved by adding 1000 ppm of DPI1, DPI2, and DPI3, respectively.
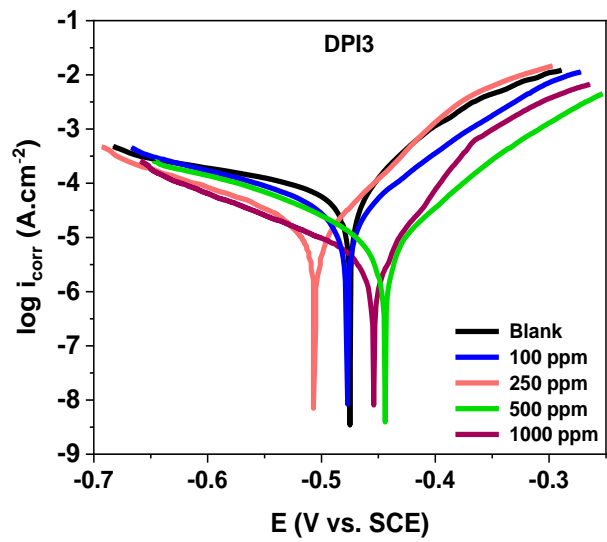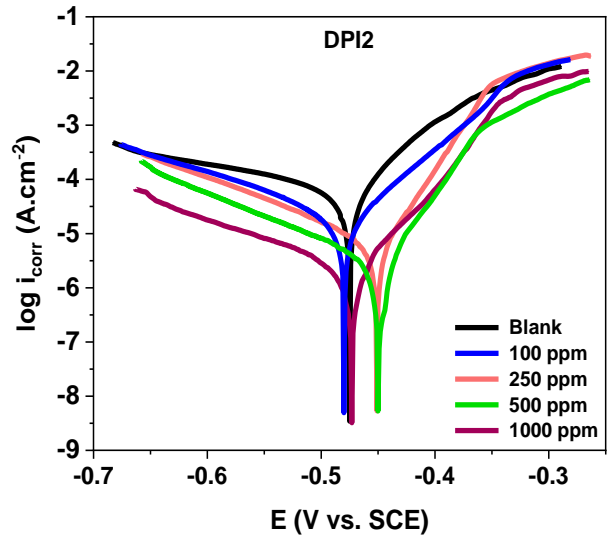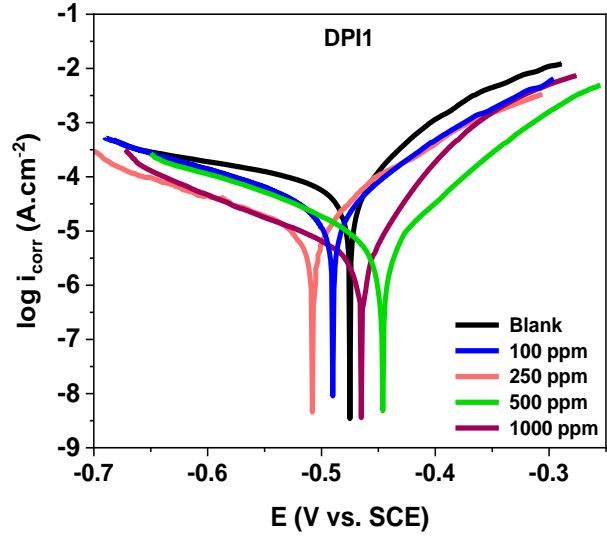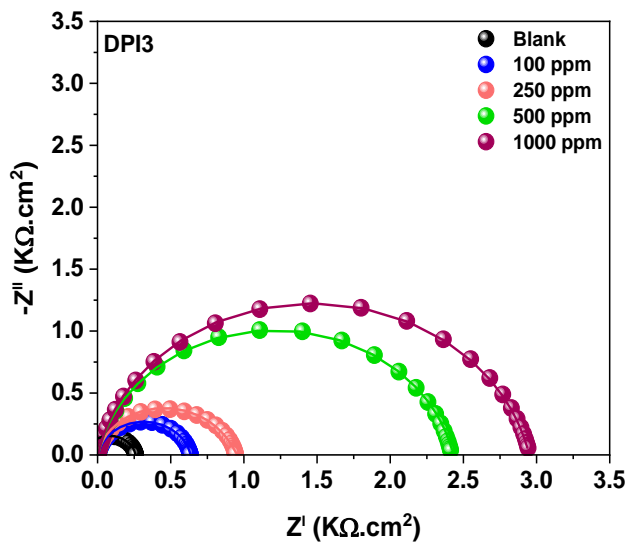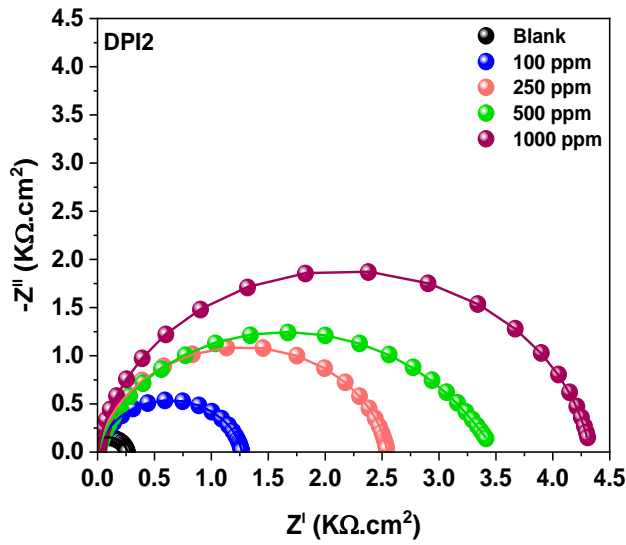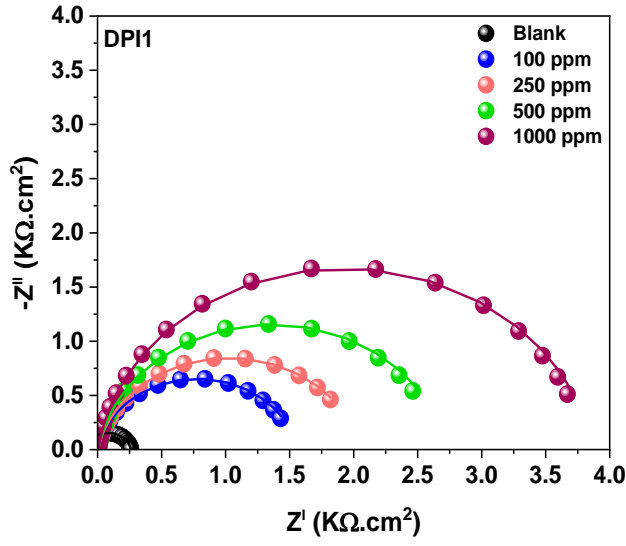
Fig. 12. PDP plots of MS in H_2S-CO_2 oilfield-produced water for blank and DPI solutions.

Table 2. PDP parameters of MS for blank and DPI solutions in the H_2S-CO_2 oilfield-produced water.

Sample	C_{inh} (ppm)	$-E_{corr}$ (mV/$_{SCE}$)	β_a (mV/dec)	$-\beta_c$ (mV/dec)	R_p (kΩ cm^2)	i_{corr} (μA cm^{-2})	CR (mpy)	η_{PDP} (%)
Blank	-	483	52	205	0.44	41.38	18.90	-
DPI1	100	491	61	137	1.06	17.32	7.91	58.2
	250	513	58	135	2.01	8.79	4.01	78.8
	500	449	48	122	3.79	3.95	1.80	90.5
	1000	469	39	111	5.18	2.42	1.11	94.2
DPI2	100	486	54	131	1.06	15.66	7.15	62.2
	250	452	42	129	2.25	6.11	2.79	85.2
	500	455	35	122	4.88	2.42	1.11	94.2
	1000	478	33	117	7.32	1.53	0.70	96.3
DPI3	100	479	54	125	1.01	16.42	7.50	60.3
	250	507	48	121	1.35	11.08	5.06	73.2
	500	451	41	119	2.17	6.12	2.79	85.2
	1000	459	34	112	3.87	2.93	1.34	92.9

3.4.2. Electrochemical impedance spectroscopy study

EIS measurements were performed to approve further the inhibition ability of DPIs to prevent MS corrosion in H_2S-CO_2 oilfield-produced water. Nyquist and Bode-phase plots of MS in the corrosive medium for blank and DPI solutions are presented in Fig. 13 and 14, respectively. In both uninhibited and inhibited solutions, the depressed semi-circles observed, and their size increased by adding DPIs to a blank medium and became more significant in higher concentrations of inhibitors (Fig. 13).

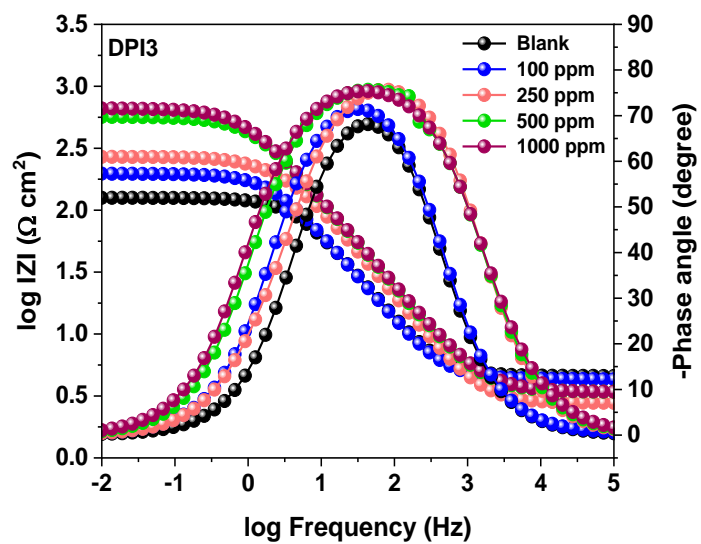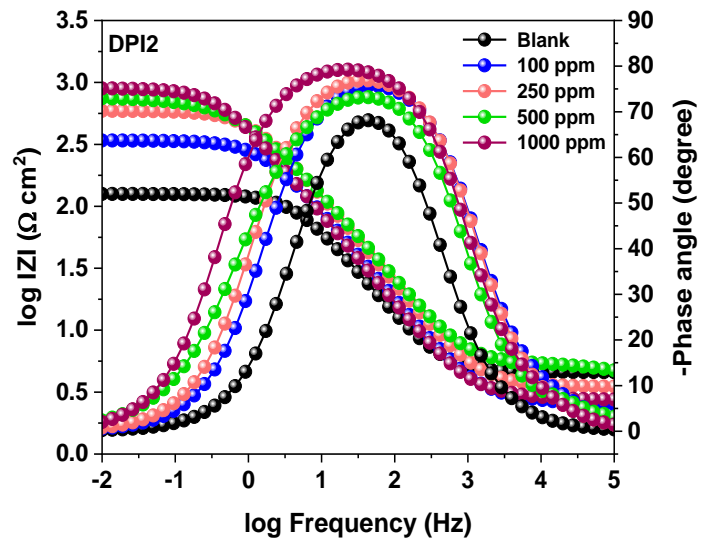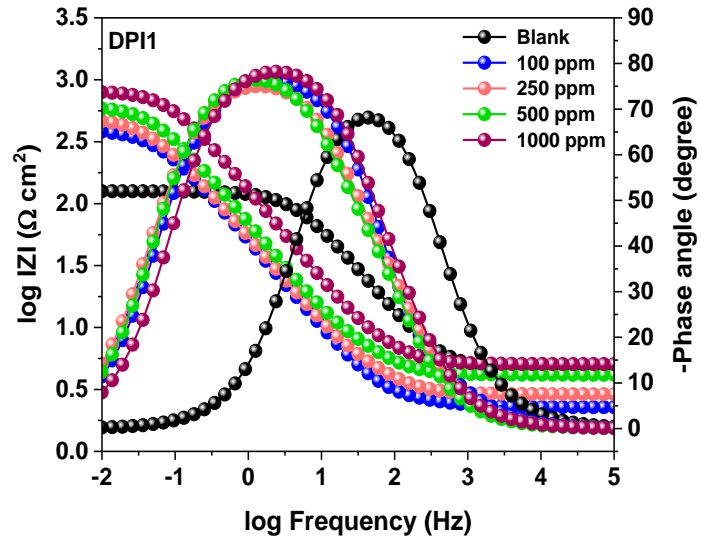**Fig. 13.** Nyquist plots of MS in H_2S-CO_2 oilfield produced water for blank and DPI solutions.

Moreover, the absolute impedance values are seen in Bode plots (Fig. 14), which raised in magnitude because of the addition of DPIs. Compared to the blank solution, broader and higher phase angle peaks are observed in the presence of DPIs. A phase angle above 70˚ could be noticed at all concentrations of DPIs, implying the enhanced resistance of MS to corrosion. Thus, the adsorption of DPI molecules on the surface of MS creates a protective layer that separates the metal surface from the corrosive environment, which leads to the larger phase angle maxima and Nyquist semi-circle diameters. EIS data were analyzed using the Randles equivalent and two-time constant circuits, respectively, for blank and DPI solutions, as shown in Fig. S2 [46,69,70]. In equivalent circuits, *CPE, R_p, R_f, R_s, R_{ct}, and CPE_f* are constant phase elements, polarization resistance, film resistance, solution resistance, charge transfer resistance, and non-ideal capacitance of the DPI film, respectively. Equation (3) defines the impedance of *CPE* (Z_{CPE}) [52]:

$$Z_{CPE} = Y_0^{-1}(j\omega)^{-n} \tag{3}$$

where *n*, Y_0, *j*, and ω represent phase shift, *CPE* constant, the imaginary unit ($j^2 = -1$), and angular frequency, respectively. The inhibition efficiency of DPI was calculated using Eq. (4) [46,70]:

$$\eta_{EIS} = \left(1 - \frac{R_0}{R}\right) \times 100 \tag{4}$$

where R_0 and *R* are, respectively, the polarization resistances for the blank and DPI solutions. All extracted fitted results of EIS tests are summarized in Table 3. The table reveals that adding DPIs to the aggressive environment increased the value of R_{ct}, especially when the inhibitor concentration reached 1000 ppm. The obtained small values of $\chi2$ confirmed the excellent fitting of Nyquist curves with the applied equivalent circuit.

Fig. 14. Bode-phase plots of MS in H_2S-CO_2 oilfield produced water for blank and DPI solutions.

DPI2 showed the best inhibition effect similar to PDP measurements and improved the value of R_{ct} from 0.25 kΩ cm^2 for the blank solution to 4.31 kΩ cm^2. However, DPI film provided the additional resistance (R_f) for MS and enhanced its total resistance. In addition, the electric double-layer capacitance and values of n decreased in the presence of DPIs, indicating that the inhibitors adsorbed on the MS surface [46,69,72]. Table 3 demonstrates that DPI1, DPI2, and DPI3 inhibited MS corrosion by 94.0%, 94.2%, and 92.0% efficiency at 1000 ppm. These results indicate that the surface of MS is covered by DPI molecules and prevents direct contact between the metal and corrosive medium, thereby inhibiting the corrosion process. The results of EIS tests are in line with PDP experiments and show that DPIs can be considered efficient inhibitors for suppressing MS corrosion in H_2S-CO_2 oilfield-produced water.

Table 3. EIS parameters of MS for blank and DPI solutions in the H_2S-CO_2 oilfield-produced water.

Sample	C_{inh} (ppm)	R_s (Ω cm^2)	R_f (Ω cm^2)	n_f	C_f (μF cm^{-2})	R_{ct} (kΩ cm^2)	n_{dl}	C_{dl} (μF cm^{-2})	η_{EIS} (%)	$\chi^2 \times 10^{-3}$
Blank	-	5.39	-	-	-	0.25	0.91	68.8	-	0.3
DPI1	100	2.29	17.91	0.90	836.5	1.54	0.78	25.3	77.1	0.5
	250	3.01	22.86	0.91	702.3	1.96	0.79	21.9	82.0	0.2
	500	4.90	41.01	0.92	668.4	2.61	0.81	18.7	86.5	0.8
	1000	6.19	47.83	0.93	302.9	3.80	0.81	16.1	94.0	0.6
DPI2	100	2.48	0.91	0.88	36.6	1.29	0.86	34.3	72.7	0.4
	250	3.82	1.23	0.91	30.5	2.53	0.87	23.8	86.1	0.1
	500	5.58	1.49	0.93	29.1	3.47	0.87	19.9	89.8	0.9
	1000	2.83	1.59	0.94	27.9	4.31	0.88	15.2	94.2	0.1
DPI3	100	4.87	13.43	0.90	55.8	0.64	0.78	8.8	45.1	0.1
	250	2.88	28.27	0.91	41.6	0.95	0.79	7.3	63.2	0.2
	500	3.69	40.76	0.92	29.6	2.41	0.79	2.3	85.4	0.5

	1000	3.72	46.73	0.92	30.1	2.96	0.80	2.1	92.0	0.2

3.4. Corrosion theoretical study

3.4.1 FMO analysis

The electro-donation and electro-acceptance interactions between the molecules and the metallic surface are determined by both HOMO and LUMO, which are crucial for inhibitor adsorption. Even though the HOMO electron density of DPI2 is primarily fixed in purlieu in carbon-oxygen bonds near the anion, as illustrated in Fig. 15, its LUMO electron density is dispersed in the nearby area of the phenyl rings of the molecule. The HOMO electron density is spread out towards the molecules' heteroatoms (O) in Fig. 15, indicating the inhibitor's capacity to deliver electrons to the iron surface. This electron sharing creates an organic barrier coating on the metal surface, which protects the metal surface from corrosion [73,74]. Another kind of electron acceptor part of DPI2, known as the LUMO, is connected with sections of the inhibitor that receive electrons from a metal surface [73,75].
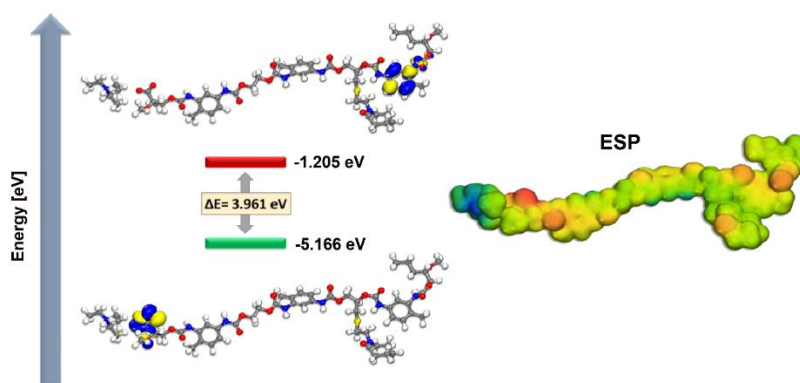
**Fig. 15.** HOMO, LUMO, and ESP surface of DPI2.

In principle, the inhibitor should reflect a little increased tendency for surface adsorption onto the metal because heteroatoms (N and O) interchange lone pair electrons with the unoccupied iron d-orbital [76]. The most frequently computed descriptors from DFT simulations are included in Table S2. These parameters are essential for better understanding the adsorptive behavior of corrosion inhibitors [74,77]. The low electron affinity and high ionization potential values of the inhibitors are commonly assumed to explain their adsorption on the Fe(110) surface, implying an equivalent inclination to exchange electrons with the metal surface (Table S2) [78]. On the other hand, high chemical softness and low hardness values indicate the adsorptive affinity of inhibitors for the metal surface. The proportion of transferred electrons (*ΔN*) of the inhibitor reveals its potential as an electron-receiving species from the Fe(110) surface [79,80]. Besides, Mulliken Atomic Charges (MAC) are reliable and credible indices of metal adsorption inhibitory sites. At the most negatively charged atom, the interaction between the Fe(110) surface and the inhibitor molecules is commonly thought to be helpful [75,78]. The MAC result for DPI2 is presented in Fig. S3. The negative charges of DPI2 on the O, N, and S atoms indicate that these centers have the highest electron density and adhere to the metal surface. This is also evident in Fig. 15, which shows the molecular electrostatic potential (MEP) of the inhibitor (area in red).

3.4.2. Monte Carlo and Molecular dynamic simulations

The interaction of DPI2 with the Fe(110) surface provides a simple method for analyzing the adsorption energetics of the system. This may be measured using the equation (9) to calculate the adsorption energy (*E*$_{ads}$)[74,81,82] :

$$E_{adsorption} = E_{Fe(110)_{||}inhibitor} - \left(Fe_{(110)} + E_{inhibitor}\right) \tag{5}$$

where $E_{Fe(110)_{\parallel}inhibitor}$ is the total energy of the simulated system, $E_{Fe,}$ and $E_{inhibitor}$ are the total energy of the Fe(110) surface and the corresponding free inhibitor molecules, respectively. After completing MC calculations, a direct analysis of the inhibitor's adsorption geometry was conducted. The steady-state energy value demonstrated that the MC simulation successfully achieved equilibrium. The system attained its minimum energy state halfway through the simulation session. Fig. 16 exhibits the actual placement of adsorbed DPI2 on a simulated Fe(110) plane derived from MC and MD simulations.
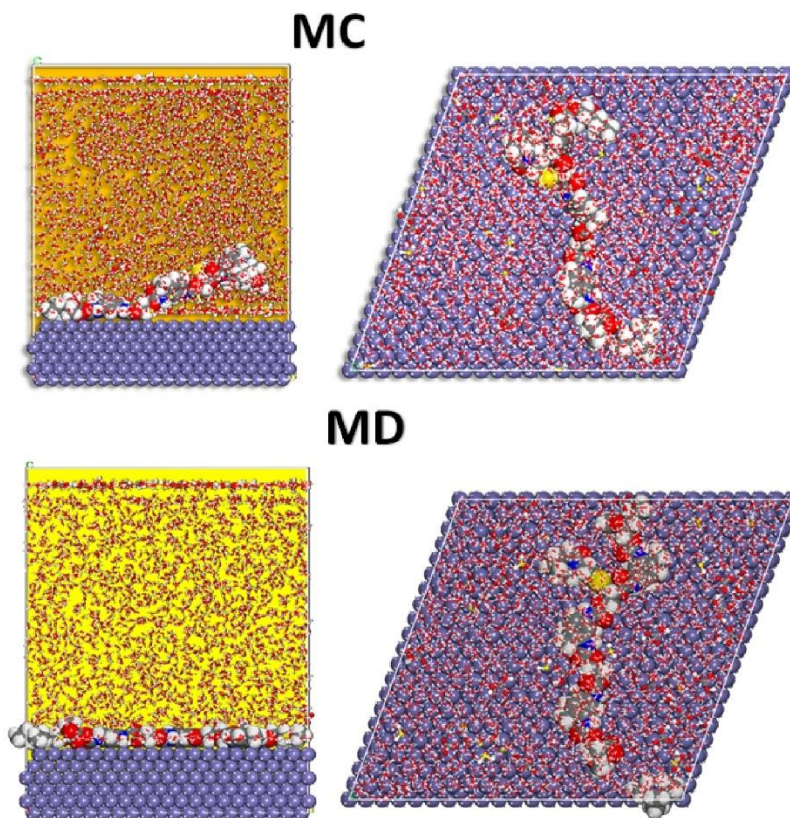
Fig. 16. MC and MD with the lowest adsorption configurations for DPI2 in the simulated corrosion media on the Fe(110) substrate.

Parallel to the inhibitor, the surface of Fe(110) is being embellished. The structure of the DPI2 molecule may be due to the backbone of the inhibitor interacting with the atoms on the surface of the Fe (110) plane, leading it to adsorb across it. This adsorptive property is caused by the tendency of a molecule to expose its heteroatoms and rich electron ring to the surface [83,84]. The E_{ads} onto the metal surface (Fig. 17a) for inhibitor adsorption is relatively high. Such high adsorption energies indicate that DPI2 and metal have a strong adsorptive relationship. This contact allows the formation of a protective layer on the metal surface that shields it from corrosion [73,75,79,80,85]. MD is commonly regarded as a more realistic description of adsorption dynamics. DPI2 adopts a very flat base onto the metal surface after several hundreds of ps of NVT simulation and is securely adsorbed onto the Fe surface. Additionally, the RDF analysis of the MD trajectory obtained during corrosion investigations has shown to be a simple way of comprehending the nature of the inhibitor adsorption process on the metal surface [73,78,80]. The type of adsorption process can be determined through the presence of peaks in the RDF graph at some distance from the metal surface. For example, the peak at distances higher than 3.5 Å and between 1-3.5 Å are expected for physisorption and chemisorption, respectively [73,79,82]. RDF of O, N, and S atoms of DPI2 on the Fe(110) surface achieved from MD trajectory analysis is displayed in Fig.17b. This example shows that the inhibitor appears to interact substantially with the metal surface, as evidenced by its comparatively high negative energy value and RDF peaks. As supported by MAC, this interaction is reliant on the O, N, and S atoms of the inhibitor.
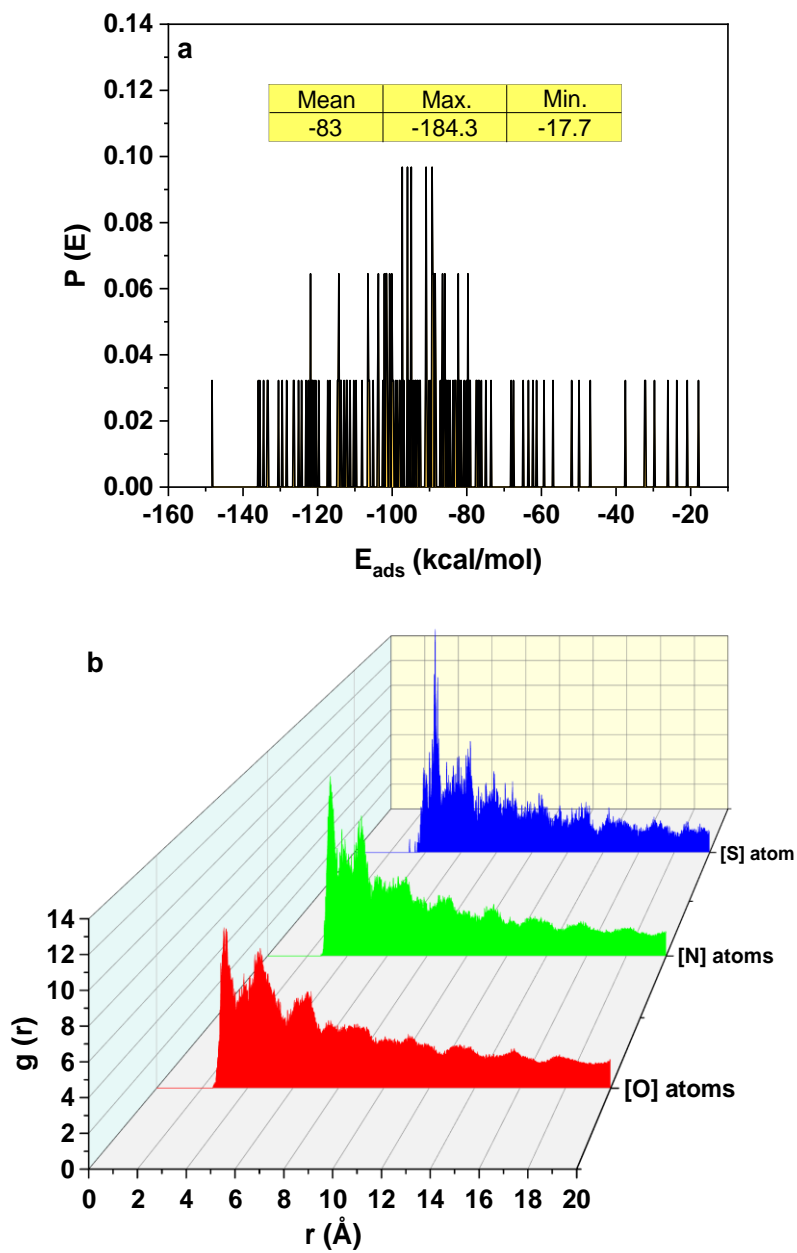
Fig. 17. The distribution of inhibitor adsorption energies in the simulated corrosive media from MC simulation (a) and RDF of heteroatoms for the inhibitor on the Fe(110) surface from MD trajectory analysis (b).

Conclusions

In this study, a hybrid inhibition method for gas hydrate formation and corrosion management was presented to reduce flow assurance operation costs in the oil and gas industry and overcome compatibility concerns between inhibitors. The findings were summarized as follows:

1. DPIs decreased the onset temperature of hydrate formation from 13.94 ˚C in uninhibited solution to 6.01 ˚C and 0.90 ˚C in the solution containing 5000 ppm of DPI1 and DPI2, respectively, which are equal to 13.0 ˚C and 18.1 ˚C subcooling temperatures.

2. The hydrate growth step of natural gas hydrate formation was affected in the presence of DPIs as they reduced the amount of gas consumption.

3. Some evidence from the MD simulation results confirmed that the DPI2 molecule behaved as an inhibitor at the hydrate surface. The tetrahedral ordering of the water molecules at the interface lowered in the presence of DPI2, implying it can be worked as an effective gas hydrate inhibitor.

4. The anion part of the inhibitor tends to interact with the water molecules around it by forming new hydrogen bonds, which lowers the order of the hydrate network and disrupts the hydrate growth process.

5. The results of corrosion measurements indicated that DPIs effectively mitigated MS corrosion in the H_2S-CO_2 oilfield-produced water. The corrosion rate of MS was reduced from 18.90 mpy for blank to 1.11, 0.70, and 1.34 mpy in the presence of DPI1, DPI2, and DPI3, respectively.

6. The inhibitors considerably improved the polarization resistance of MS up to 7.32 kΩ cm^2 with the highest inhibition efficiency of 96.3%.

7. The simulation results revealed that phenyl rings and heteroatoms in the DPI structure played the main role in its adsorption on the MS surface. The adsorption energy of DPI2

on the metal surface was very high, which allowed the formation of a protective layer on the metal surface to shield it from corrosion.

These results indicate that the design of a single inhibitor that contains active functional groups for both gas hydrate and corrosion inhibition can be considered a promising strategy for flow assurance applications.

Acknowledgment

References

[1]   Guo B, Song S, Ghalambor A, Lin TR. Offshore pipelines: design, installation, and maintenance. Gulf Professional Publishing; 2013.

[2]   YONG BAI. Subsea engineering handbook. Elsevier Science; 2010.

[3]   Wasden FK. Flow assurance in deepwater flowlines and pipelines-challenges met, challenges remaining. Offshore Technol. Conf., Offshore Technology Conference; 2003.

[4]   Kelland MA. Production chemicals for the oil and gas industry. CRC press; 2014.

[5]   Hassanpouryouzband A, Joonaki E, Farahani MV, Takeya S, Ruppel C, Yang J, et al. Gas hydrates in sustainable chemistry. Chem Soc Rev 2020;49:5225–309.

[6]   Farhadian A, Naeiji P, Varfolomeev MA, Peyvandi K, Kiiamov AG. Reconsideration of the micellization theory: Promotion or inhibition of gas hydrate formation for gas storage and flow assurance applications. Chem Eng J 2022;427:131852.

[7]   Sloan ED, Koh CA. Clathrate hydrates of natural gases. CRC Press 3rd Ed; CRC Press (Taylor Fr Group) 2008;87.

[8]   Lee D, Jeoung S, Moon HR, Seo Y. Recoverable and recyclable gas hydrate inhibitors based on magnetic nanoparticle-decorated metal–organic frameworks. Chem Eng J 2020;401:126081.

[9]   Li W, De Qing L. Inhibition effects of poly (N-vinylcaprolactam)/poly (ε-caprolactone) amphiphilic block copolymers on methane hydrate formation. J Ind Eng Chem 2021;96:183–93.

[10]   Zhou X, Zhang Q, Long Z, Liang D. In situ PXRD analysis on the kinetic effect of PVP-K90 and PVCap on methane hydrate dissociation below ice point. Fuel 2021;286:119491.

[11]   Farhadian A, Shadloo A, Zhao X, Pavelyev RS, Peyvandi K, Qiu Z, et al. Challenges and advantages of using environmentally friendly kinetic gas hydrate inhibitors for flow assurance application: A comprehensive review. Fuel 2023;336:127055.

[12]   Farhadian A, Varfolomeev MA, Shaabani A, Zaripova YF, Yarkovoi V V., Khayarov KR. Inhibition Performance of Chitosan- graft-Polyacrylamide as an Environmentally Friendly and High-Cloud-Point Inhibitor of Nucleation and Growth of Methane Hydrate. Cryst Growth Des 2020;20:1771–8.

[13]   Farhadian A, Kudbanov A, Varfolomeev MA, Dalmazzone D. Waterborne Polyurethanes as a New and Promising Class of Kinetic Inhibitors for Methane Hydrate Formation. Sci Rep 2019;9:9797.

[14]   Farhadian A, Kashani SA, Rahimi A, Oguzie EE, Javidparvar AA, Nwanonenyi SC, et al.

Modified hydroxyethyl cellulose as a highly efficient eco-friendly inhibitor for suppression of mild steel corrosion in a 15% HCl solution at elevated temperatures. J Mol Liq 2021;338:116607.

[15]   Lu Y, Yuan C, Wang H, Yang L, Zhang L, Zhao J, et al. Atomistic insights into the performance of thermodynamic inhibitors in the nucleation of methane hydrate. Chem Eng J 2021;431:133479.

[16]   Deka B, Barifcani A, Al Helal A, Badi D, Mahto V, Vuthaluru H. Generation of methane gas hydrate equilibrium curve for the thermodynamic gas hydrate inhibitor propylene glycol. J Pet Sci Eng 2021;199:108312.

[17]   Farhadian A, Varfolomeev MA, Kudbanov A, Rezaeisadat M, Nurgaliev DK. Waterborne polymers as kinetic/anti-agglomerant methane hydrate and corrosion inhibitors: a new and promising strategy for flow assurance. J Nat Gas Sci Eng 2020;77:103235.

[18]   Zhao Y, Liu Y, Dong H, Chen C, Zhang T, Yang L, et al. Synthesis and Application of Magnetically Recyclable Nanoparticles as Hydrate Inhibitors. Chem Eng J 2021;431:133966.

[19]   Go W, Lee D, Seo Y. Synergistic inhibition effects of hydrophilic monomeric substances on CH4 hydrate as revealed by experimental and computational approaches. Chem Eng J 2021;426:130794.

[20]   Das S, Mahto V, Udayabhanu G, Lall M V, Singh K, Deepak M. Experimental evaluation of Sarcosine as an eco-friendly green hydrate inhibitor for the drilling of gas hydrate bearing formations. J Pet Sci Eng 2021:109764.

[21]   Kelland MA. Challenges with gas hydrate formation. IOP Conf. Ser. Mater. Sci. Eng., vol. 700, IOP Publishing; 2019, p. 12057.

[22]   Singh A, Suri A. Review of Kinetic Hydrate Inhibitors Based on Cyclic Amides and Effect of Various Synergists. Energy and Fuels 2021;35:15301–38.

[23]   Zhang Q, Kelland MA. A new investigation of polymaleamides as kinetic hydrate inhibitors–Improved performance and compatibility with high salinity brines. Chem Eng Sci 2021;241:116719.

[24]   Liu Y, Zhao Y, Jia Y, Zhang L, Yang L, Zhao J. Understanding the inhibition performance of kinetic hydrate inhibitors in nanoclay systems. Chem Eng J 2021;424:130303.

[25]   Noh H-J, Lee D, Go W, Choi G, Im Y-K, Mahmood J, et al. Fused aromatic networks as a new class of gas hydrate inhibitors. Chem Eng J 2021:133691.

[26]   Kelland MA, Zhang Q, Dirdal EG, Mady MF. Reliability and Performance of Vinyl Lactam-Based Kinetic Hydrate Inhibitor Polymers after Treatment under a Range of Conditions. Energy & Fuels 2021;35:1273–80.

[27]   Liu Y, Wang X, Lang C, Zhao J, Lv X, Ge Y, et al. Experimental study on the gas hydrates blockage and evaluation of kinetic inhibitors using a fully visual rocking cell. J Nat Gas Sci Eng 2021;96:104331.

[28]   Ghosh R, Kelland MA. Pushing the Known Performance Envelope of Kinetic Hydrate Inhibitors─ Powerful Synergy of Trialkylamine Oxides with Acrylamide-based Polymers. Energy & Fuels 2021;36:341–349.

[29]   Zhang Q, Limmer L, Frey H, Kelland MA. N-Oxide Polyethers as Kinetic Hydrate

Inhibitors: Side Chain Ring Size Makes the Difference. Energy & Fuels 2021;35:4067–74.

[30] Farhadian A, Varfolomeev MA, Kudbanov A, Gallyamova SR. A new class of promising biodegradable kinetic/anti-agglomerant methane hydrate inhibitors based on castor oil. Chem Eng Sci 2019;206:507–17.

[31] Shi L, He Y, Lu J, Liang D. Effect of dodecyl dimethyl benzyl ammonium chloride on CH4 hydrate growth and agglomeration in oil-water systems. Energy 2020;212:118746.

[32] Shi L, He Y, Lu J, Hou G, Liang D. Anti-agglomeration evaluation and Raman spectroscopic analysis on mixed biosurfactants for preventing CH4 hydrate blockage in n-octane+ water systems. Energy 2021;229:120755.

[33] Zhao X, Fang Q, Qiu Z, Mi S, Wang Z, Geng Q, et al. Experimental investigation on hydrate anti-agglomerant for oil-free systems in the production pipe of marine natural gas hydrates. Energy 2022;242:122973.

[34] Wang Y, Koh CA, White J, Patel Z, Zerpa LE. Hydrate formation management simulations with anti-agglomerants and thermodynamic inhibitors in a subsea tieback. Fuel 2019;252:458–68.

[35] Sa J-H, Sum AK. Advancing Laboratory Characterization and Qualification of Additives for Hydrate Slurry Flow in Multiphase Systems. Ind Eng Chem Res 2020;60:719–28.

[36] Eduok U, Szpunar J. Corrosion Inhibitors for Sweet Oilfield Environment (CO 2 Corrosion). Corros Inhib Oil Gas Ind 2020:177–227.

[37] Eduok U, Szpunar J. Corrosion Inhibitors in the Oil and Gas Industry. Wiley Online Library; 2020.

[38] Rahimi A, Abdouss M, Farhadian A, Guo L, Kaya S, Neshati J. Enhancement corrosion resistance of mild steel in 15% HCl solution by a novel bio-based polyurethane for oil well acidizing. J Ind Eng Chem 2022;113:332–47.

[39] Rahimi A, Abdouss M, Farhadian A, Guo L, Neshati J. Development of a Novel Thermally Stable Inhibitor Based on Furfuryl Alcohol for Mild Steel Corrosion in a 15% HCl Medium for Acidizing Application. Ind Eng Chem Res 2021;60:11030–11044.

[40] Farhadian A, Rahimi A, Safaei N, Shaabani A, Sadeh E, Abdouss M, et al. Exploration of Sunflower Oil As a Renewable Biomass Source to Develop Scalable and Highly Effective Corrosion Inhibitors in a 15% HCl Medium at High Temperatures. ACS Appl Mater Interfaces 2021;13.

[41] Chauhan DS, Quraishi MA, Qurashi A. Recent trends in environmentally sustainable Sweet corrosion inhibitors. J Mol Liq 2021;326:115117.

[42] Rahimi A, Farhadian A, Berisha A, Shaabani A, Varfolomeev MA, Mehmeti V, et al. Novel sucrose derivative as a thermally stable inhibitor for mild steel corrosion in 15% HCl medium: An experimental and computational study. Chem Eng J 2022;446:136938.

[43] Lei X, Wang H, Mao F, Zhang J, Zhao M, Fu A, et al. Electrochemical behaviour of martensitic stainless steel after immersion in a H2S-saturated solution. Corros Sci 2018;131:164–73.

[44] Farimani AM, Hassannejad H, Nouri A, Barati A. Using oral penicillin as a novel environmentally friendly corrosion inhibitor for low carbon steel in an environment containing hydrogen sulfide corrosive gas. J Nat Gas Sci Eng 2020;77:103262.

[45]   Javidi M, Haghshenas SMS, Shariat MH. CO2 corrosion behavior of sensitized 304 and 316 austenitic stainless steels in 3.5 wt.% NaCl solution and presence of H2S. Corros Sci 2020;163:108230.

[46]   Zhang QH, Hou BS, Zhang GA. Inhibitive and adsorption behavior of thiadiazole derivatives on carbon steel corrosion in CO2-saturated oilfield produced water: Effect of substituent group on efficiency. J Colloid Interface Sci 2020;572:91–106.

[47]   Davoodi A, Pakshir M, Babaiee M, Ebrahimi GR. A comparative H2S corrosion study of 304L and 316L stainless steels in acidic media. Corros Sci 2011;53:399–408.

[48]   Ismail MC, Yahya S, Raja PB. Antagonistic effect and performance of CO2 corrosion inhibitors: Water chemistry and ionic response. J Mol Liq 2019;293:111504.

[49]   Zhang C, Zhao J. Effects of pre-corrosion on the corrosion inhibition performance of three inhibitors on Q235 steel in CO2/H2S saturated brine solution. Int J Electrochem Sci 2017;12:9161–79.

[50]   Obanijesu EO, Pareek V, Tade MO. Hydrate formation and its influence on natural gas pipeline internal corrosion rate. SPE oil gas India Conf. Exhib., OnePetro; 2010.

[51]   Aslam J, Aslam R, Zehra S, Rizvi M. Corrosion inhibitors for sweet (CO2 corrosion) and sour (H2S corrosion) oilfield environments. Environ. Sustain. Corros. Inhib., Elsevier; 2022, p. 165–81.

[52]   Farhadian A, Go W, Yun S, Rahimi A, Nabid MR, Iravani D, et al. Efficient dual-function inhibitors for prevention of gas hydrate formation and CO2/H2S corrosion inside oil and gas pipelines. Chem Eng J 2021;431:134098.

[53] Farhadian A, Varfolomeev MA, Shaabani A, Nasiri S, Vakhitov I, Zaripova YF, et al. Sulfonated chitosan as green and high cloud point kinetic methane hydrate and corrosion inhibitor: Experimental and theoretical studies. Carbohydr Polym 2020;236:116035.

[54] Farhadian A, Varfolomeev MA, Semenov AP, Mendgaziev RI, Stoporev AS. Dual-Function Synergists Based on Glucose and Sucrose for Gas Hydrate and Corrosion Inhibition. Energy & Fuels 2020;34:13717–13727.

[55] Farhadian A, Varfolomeev MA, Rahimi A, Mendgaziev RI, Semenov AP, Stoporev AS, et al. Gas Hydrate and Corrosion Inhibition Performance of the Newly Synthesized Polyurethanes: Potential Dual Function Inhibitors. Energy & Fuels 2021;35:6113–24.

[56] Farhadian A, Varfolomeev MA, Rezaeisadat M, Semenov AP, Stoporev AS. Toward a bio-based hybrid inhibition of gas hydrate and corrosion for flow assurance. Energy 2020;210:118549.

[57] He Y, Sun M-T, Chen C, Zhang G-D, Chao K, Lin Y, et al. Surfactant-based promotion to gas hydrate formation for energy storage. J Mater Chem A 2019;7:21634–61.

[58] Qasim A, Khan MS, Lal B, Shariff AM. A perspective on dual purpose gas hydrate and corrosion inhibitors for flow assurance. J Pet Sci Eng 2019;183:106418–40.

[59] Omrani I, Farhadian A, Babanejad N, Shendi HK, Ahmadi A, Nabid MR. Synthesis of novel high primary hydroxyl functionality polyol from sunflower oil using thiol-yne reaction and their application in polyurethane coating. Eur Polym J 2016;82:220–31.

[60] Tang C, Farhadian A, Berisha A, Deyab MA, Chen J, Iravani D, et al. Novel Biosurfactants for Effective Inhibition of Gas Hydrate Agglomeration and Corrosion in Offshore Oil and

Gas Pipelines. ACS Sustain Chem Eng 2022.

[61] Abrahamsen E, Kelland MA. Comparison of kinetic hydrate inhibitor performance on structure I and structure II hydrate-forming gases for a range of polymer classes. Energy & Fuels 2018;32:342–51.

[62] Zhang Q, Kelland MA, Ajiro H. Polyvinylsulfonamides as Kinetic Hydrate Inhibitors. Energy Fuels 2020;34:2230–7.

[63] Ree LS, Sirianni Q, Gillies ER, Kelland MA. A Systematic Study of Polyglyoxylamides as Powerful, High Cloud Point Kinetic Hydrate Inhibitors. Energy Fuels 2019;33:2067–2075.

[64] Abrahamsen E, Kelland MA. Carbamate Polymers as Kinetic Hydrate Inhibitors. Energy Fuels 2016;30:8134–40.

[65] Zhang Q, Kawatani R, Ajiro H, Kelland MA. Optimizing the Kinetic Hydrate Inhibition Performance of N-Alkyl-N-vinylamide Copolymers. Energy Fuels 2018;32:4925–31.

[66] Kelland MA, Abrahamsen E, Ajiro H, Akashi M. Kinetic hydrate inhibition with N-alkyl-N-vinylformamide polymers: comparison of polymers to n-propyl and isopropyl groups. Energy Fuels 2015;29:4941–6.

[67] Mady MF, Kelland MA. N, N -dimethylhydrazidoacrylamides. Part 2: High-cloud-point kinetic hydrate inhibitor copolymers with n - Vinylcaprolactam and effect of ph on performance. Energy Fuels 2015;29:678–85.

[68] Bagherzadeh SA, Alavi S, Ripmeester JA, Englezos P. Why ice-binding type I antifreeze protein acts as a gas hydrate crystal inhibitor. Phys Chem Chem Phys 2015;17:9984–90.

[69] Solomon MM, Onyeachu IB, Njoku DI, Nwanonenyi SC, Oguzie EE. Adsorption and

corrosion inhibition characteristics of 2–(chloromethyl) benzimidazole for C1018 carbon steel in a typical sweet corrosion environment: effect of chloride ion concentration and temperature. Colloids Surfaces A Physicochem Eng Asp 2021;610:125638.

[70] Onyeachu IB, Obot IB, Sorour AA, Abdul-Rashid MI. Green corrosion inhibitor for oilfield application I: Electrochemical assessment of 2-(2-pyridyl) benzimidazole for API X60 steel under sweet environment in NACE brine ID196. Corros Sci 2019;150:183–93.

[71] Farhadian A, Rahimi A, Safaei N, Shaabani A, Abdouss M, Alavi A. A Theoretical and Experimental Study of Castor oil-based inhibitor for Corrosion Inhibition of Mild Steel in Acidic Medium at Elevated Temperatures. Corros Sci 2020;175:108871.

[72] Saleh TA, Haruna K, Mohammed A-RI. Octanoate grafted graphene oxide as an effective inhibitor against oil well acidizing corrosion. J Mol Liq 2021;325:115060.

[73] Hsissou R, Benhiba F, Abbout S, Dagdag O, Benkhaya S, Berisha A, et al. Trifunctional epoxy polymer as corrosion inhibition material for carbon steel in 1.0 M HCl: MD simulations, DFT and complexation computations. Inorg Chem Commun 2020;115:107858.

[74] Dagdag O, Hsissou R, El Harfi A, Berisha A, Safi Z, Verma C, et al. Fabrication of polymer based epoxy resin as effective anti-corrosive coating for steel: Computational modeling reinforced experimental studies. Surfaces and Interfaces 2020;18:100454.

[75] Mehmeti V V., Berisha AR. Corrosion study of mild steel in aqueous sulfuric acid solution using 4-methyl-4h-1,2,4-triazole-3-thiol and 2-mercaptonicotinic acid-an experimental and theoretical study. Front Chem 2017;AUG.

[76] Fouda AS, Ellithy AS. Inhibition effect of 4-phenylthiazole derivatives on corrosion of 304L stainless steel in HCl solution. Corros Sci 2009;51:868–75.

[77] Dagdag O, Berisha A, Safi Z, Dagdag S, Berrani M, Jodeh S, et al. Highly durable macromolecular epoxy resin as anticorrosive coating material for carbon steel in 3% NaCl: Computational supported experimental studies. J Appl Polym Sci 2020;137.

[78] Hsissou R, Abbout S, Seghiri R, Rehioui M, Berisha A, Erramli H, et al. Evaluation of corrosion inhibition performance of phosphorus polymer for carbon steel in [1 M] HCl: Computational studies (DFT, MC and MD simulations). J Mater Res Technol 2020.

[79] Dagdag O, Berisha A, Safi Z, Hamed O, Jodeh S, Verma C, et al. DGEBA-polyaminoamide as effective anti-corrosive material for 15CDV6 steel in NaCl medium: Computational and experimental studies. J Appl Polym Sci 2020;137:48402.

[80] Hsissou R, Abbout S, Berisha A, Berradi M, Assouag M, Hajjaji N, et al. Experimental, DFT and molecular dynamics simulation on the inhibition performance of the DGDCBA epoxy polymer against the corrosion of the E24 carbon steel in 1.0 M HCl solution. J Mol Struct 2019;1182:340–51.

[81] Guo L, Zhang ST, Li WP, Hu G, Li X. Experimental and computational studies of two antibacterial drugs as corrosion inhibitors for mild steel in acid media. Mater Corros 2014;65:935–42.

[82] Hsissou R, Dagdag O, Abbout S, Benhiba F, Berradi M, El Bouchti M, et al. Novel derivative epoxy resin TGETET as a corrosion inhibition of E24 carbon steel in 1.0 M HCl solution. Experimental and computational (DFT and MD simulations) methods. J Mol Liq 2019;284:182–92.

[83]   Dagdag O, Hsissou R, El Harfi A, Safi Z, Berisha A, Verma C, et al. Epoxy resins and their zinc composites as novel anti-corrosive materials for copper in 3% sodium chloride solution: Experimental and computational studies. J Mol Liq 2020;315:113757.

[84]   Jessima SJHMHM, Berisha A, Srikandan SSSS, Subhashini S. Preparation, characterization, and evaluation of corrosion inhibition efficiency of sodium lauryl sulfate modified chitosan for mild steel in the acid pickling process. J Mol Liq 2020;320:114382.

[85]   Guo L, Qi C, Zheng X, Zhang R, Shen X, Kaya S. Toward understanding the adsorption mechanism of large size organic corrosion inhibitors on an Fe(110) surface using the DFTB method. RSC Adv 2017;7:29042–50.